

Modeling the Luminosity-dependent Pulse Profile and Emission Geometry of SMC X-2 during a Giant Outburst

Ankur Roy, Rigel Cappallo, Silas G. T. Laycock, Dimitris M. Christodoulou, Georgios Vasilopoulos, Sayantan Bhattacharya

▶ **To cite this version:**

Ankur Roy, Rigel Cappallo, Silas G. T. Laycock, Dimitris M. Christodoulou, Georgios Vasilopoulos, et al.. Modeling the Luminosity-dependent Pulse Profile and Emission Geometry of SMC X-2 during a Giant Outburst. The Astrophysical Journal, 2022, 936, 10.3847/1538-4357/ac82b6 . insu-03781183

HAL Id: insu-03781183

https://insu.hal.science/insu-03781183

Submitted on 22 Sep 2022

HAL is a multi-disciplinary open access archive for the deposit and dissemination of scientific research documents, whether they are published or not. The documents may come from teaching and research institutions in France or abroad, or from public or private research centers.

L'archive ouverte pluridisciplinaire **HAL**, est destinée au dépôt et à la diffusion de documents scientifiques de niveau recherche, publiés ou non, émanant des établissements d'enseignement et de recherche français ou étrangers, des laboratoires publics ou privés.



Distributed under a Creative Commons Attribution 4.0 International License

The Astrophysical Journal, 936:90 (16pp), 2022 September 1 https://doi.org/10.3847/1538-4357/ac82b6
© 2022. The Author(s). Published by the American Astronomical Society.
OPEN ACCESS

Modeling the Luminosity-dependent Pulse Profile and Emission Geometry of SMC X-2 during a Giant Outburst

Ankur Roy[1,2], Rigel Cappallo[3], Silas G. T. Laycock[1,2], Dimitris M. Christodoulou[4], Georgios Vasilopoulos[5,6], and Sayantan Bhattacharya[1,2]
[1] Department of Physics and Applied Physics, University of Massachusetts, Lowell, MA 01854, USA; ankur_roy@student.uml.edu
[2] Lowell Center for Space Science and Technology, UMass Lowell, MA 01854, USA
[3] Massachusetts Institute of Technology, Haystack Observatory, Westford, MA 01886, USA
[4] Department of Mathematics, University of Massachusetts, Lowell, MA 01854, USA
[5] Department of Astronomy, Yale University, PO Box 208101, New Haven, CT 06520-8101, USA
[6] Université de Strasbourg, CNRS, Observatoire astronomique de Strasbourg, UMR 7550, F-67000, Strasbourg, France
Received 2022 February 5; revised 2022 July 15; accepted 2022 July 18; published 2022 September 5

Abstract

One of the brightest X-ray pulsars in the Small Magellanic Cloud is SMC X-2. During its most recent major outburst in 2015, this transient pulsar displayed significant changes in both its accretion state and magnetosphere, particularly when it entered the low-luminosity regime of subcritical accretion. Polestar is a pulse-profile modeling code that helps in delineating the geometry of the emission as the source evolves past outburst and toward lower-luminosity states. Applying Polestar to XMM-Newton and NuSTAR pulse profiles, we constrained the most likely inclination of the spin axis of the pulsar to be $i = 87° \pm 4°$. As the X-ray luminosity declined, an increase in the pulsed fraction was detected from Swift observations, which suggests a transition from fan- to pencil-beam emission during the later stages of the outburst. Additionally, we also performed analysis of the OGLE IV light curves, which showed strong modulation in the optical profiles during the outburst.

Unified Astronomy Thesaurus concepts: High mass x-ray binary stars (733); Pulsars (1306); Small Magellanic Cloud (1468); Accretion (14)

1. Introduction

The transient X-ray pulsar (XRP) SMC X-2 is in the Small Magellanic Cloud (SMC) with a maximum observed X-ray luminosity of $L_X \sim 5.5 \times 10^{38}$ erg s^{-1} in the 1–70 keV band (Jaisawal & Naik 2016). It sits at a distance of ∼62.44 kpc (Graczyk et al. 2020) with a spin period of ∼2.37 s. It is one of the earliest extragalactic X-ray sources to be identified, having been discovered in 1977 by SAS 3 (Clark et al. 1978). This XRP initially displayed a hard power-law spectral component with an X-ray luminosity on the order of 10^{38} erg s^{-1} in the energy range of 2–11 keV. It was detected for a second time during pointed ROSAT observations in 1992, identified as RX J0054.5–7340 (Kahabka & Pietsch 1996; Sasaki et al. 2000), although with a weaker X-ray luminosity by a factor of 3. Its designation as an XRP was confirmed during the RXTE SMC monitoring project (Laycock et al. 2005) in 2000, when it was observed during a type II (giant) outburst from January to April, revealing a spin period of 2.371532(2) s (Corbet et al. 2001) with $L_X > 10^{38}$ erg s^{-1}. The RXTE pulse profiles presented a distinct double-peaked feature throughout the outburst. Subsequent ASCA observations by Yokogawa et al. (2001) corroborated this result while increasing precision on the source coordinates. These authors detected single-peaked profiles at energies below 6 keV, which evolved into more complex structures above 6.0 keV including traces of double-peaked features.

The optical companion was initially resolved as a pair of stars separated by 2.5″ (Murdin et al. 1979). Both stars were systematically studied by Schurch et al. (2011) using archival OGLE III data (Udalski et al. 2008). The photometric variations of the brighter star led them to report the orbital period of the system as $P_{\rm orb} \sim 18.62 \pm 0.02$ days. Later, pulse period evolution studies by both Townsend et al. (2011) and La Palombara et al. (2016) constrained the X-ray orbital period to roughly 18.38 days, which is in sufficient agreement with the optical periodicity, confirming the optical counterpart.

During 2015, the SMC X-2 system again underwent a type II outburst. It was first detected by MAXI (Negoro et al. 2015) and then subsequently by INTEGRAL (Fotopoulou et al. 2015) and Swift (Kennea et al. 2015) . Follow-up observations by XMM-Newton and NuSTAR in their respective energy bands showed that the X-ray luminosity again reached $L_X \sim 10^{38}$ erg s^{-1}. La Palombara et al. (2016) found that although the XMM-Newton spectra were dominated by a hard cutoff power law, the spectral fit was further improved with the addition of soft thermal components. The authors suggested that this blackbody emission originates from the reprocessing of X-rays from the inner edge of the accretion disk at temperatures corresponding to $kT_B = 135$ eV. They observed double-peaked pulse profiles across the broad energy range from 0.15 to 12 keV. The NuSTAR profiles (Jaisawal & Naik 2016) showed the same double-peaked features, although in its last observation around 2015 October, the depth between the peaks became shallower and slowly started to form a single broad peak. A resurgence of single-peaked features was seen in the profiles following this observation, once with XMM-Newton and in some Swift profiles. Although Li et al. (2016) suggested that the single-peaked Swift profiles might be a result of low photon statistics, this shape transition may instead indicate a change in X-ray emission and beam pattern during the outburst. From the follow-up NuSTAR observations, a cyclotron line was detected

Original content from this work may be used under the terms of the Creative Commons Attribution 4.0 licence. Any further distribution of this work must maintain attribution to the author(s) and the title of the work, journal citation and DOI.

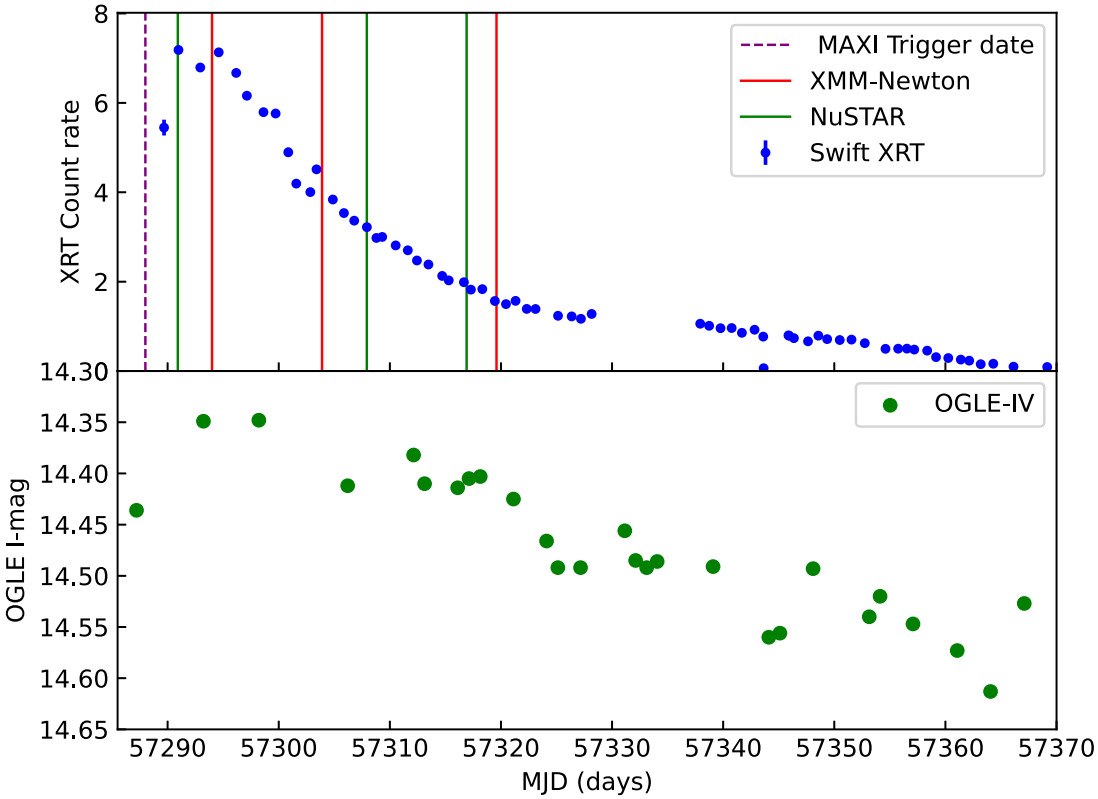


Figure 1. Top: Swift/XRT light curve for SMC X-2 during the 2015 outburst. The purple dashed line represents the date of the reported trigger (MJD 57288; Negoro et al. 2015), detected by MAXI. Superimposed on it are the different XMM-Newton and NuSTAR observations during the outburst. Bottom: simultaneous OGLE IV monitoring during the same period. We can observe a fluctuation in the optical brightness after the trigger date.

at $\sim$27 keV, implying a magnetic field of $\sim 3 \times 10^{12}$ G (Jaisawal & Naik 2016). This value was later confirmed by Lutovinov et al. (2017), who derived it empirically from the knowledge of the limiting luminosity when the source descended into the propeller regime. This determination was based solely on the Swift/XRT pointed observations, which surveyed the outburst throughout its evolution. Figure 1 presents the simultaneous X-ray and optical photometric variations during the 3 months following the X-ray outburst first detected by MAXI.

1.1. The Accretion Mechanism

In an X-ray binary, some matter from the optical companion becomes gravitationally bound to the neutron star (NS) and is consequently funneled via magnetic field lines toward the footprint on the NS surface. During this process, the potential energy of the infalling matter is converted to kinetic energy, emitting significantly in X-rays. As the accretion rate increases, an optically thick column of free-falling matter begins to form at the magnetic poles. When the radiation pressure of the incoming photons surpasses the magnetic pressure, the photons start to diffuse tangentially to the surface, thus bending the magnetic field lines, and a polar mound is created on top of the hot spot (Basko & Sunyaev 1975, 1976; Becker & Wolff 2007). As the mass transfer rate increases, a bow shock develops, and an accretion column begins to form between this shock and the NS surface. At higher luminosities, the height of this bow shock increases. In the accretion rate regime $\dot{M} < 10^{17}$ g s^{-1}, the dominant X-ray emission is pencil-beam, which emits primarily along the magnetic axis, normal to the NS surface. With increasing accretion rates, fan-beam emission begins, which is directed perpendicular to the magnetic axis and thus parallel to the NS surface. These beaming patterns are dependent on the electrons scattering off of the X-ray photons and dictate their direction of outflow (Basko & Sunyaev 1976). Thus, there exists a critical luminosity level $L_{\rm crit}$ that demarcates the two emission regimes (Becker et al. 2012). Above this critical level, the emission starts to flow through the sidewalls of the column and emerges as fan-beam radiation (Lyubarskii 1986), while below this level, it is primarily pencil-beam emission.

1.2. Motivation for the Following Analysis

The primary aim of this analysis is to determine the spin inclination angle and model the emission geometry of SMC X-2 throughout the 2015 outburst using the pulse-profile modeling code Polestar (Cappallo et al. 2017). Polestar is a vector-based, geometrical model that incorporates pencil- and fan-beam emission contributions from two hot spots on a rotating NS. Through modeling the features of pulse profiles, it attempts to constrain the inclination and magnetic dipole axis angle of a given XRP. Polestar has been previously applied to two other pulsars in the SMC, namely, SXP 348 (Cappallo et al. 2019) and SXP 1062 (Cappallo et al. 2020). Here we apply the same geometric model for the first time on profiles observed during a type II outburst.

The content of this paper is arranged as follows. In Section 2, we describe about the different data sets that we worked with and our analysis methods. In Section 3, we present results from Polestar analysis along with additional X-ray analysis. Following this, Sections 4 and 5 include the discussion and conclusions of our results, respectively.

2. Observations and Methodology

2.1. XMM-Newton

The source was detected three times during the 2015 outburst by XMM-Newton (Jansen et al. 2001), all within 1 month of each other. It was detected by the pn camera (Strüder et al. 2001), once in timing mode and in imaging mode for the other two observations. We extracted the data from the XMM-Newton Science Archive[7] server. For the mission specific tasks, we used the Science Analysis Software (SAS) version 17.0.0. The pn light curves (pattern $\leqslant$ 4, single- and double-pixel events) were extracted in the 0.2–12 keV energy range from cleaned event files and corrected for good time intervals by using the recommended threshold rate values for EPIC-pn.[8] For ObsID 0770580701, we used the standard analysis procedures[9] to obtain the light curves in the timing mode. La Palombara et al. (2016) suggested evidence of a pileup happening on the pn CCDs in ObsID 0770580801. Subsequently, we followed their prescription for extracting photons from an annulus of inner and outer radii of 10″ and 45″ to account for mild pileup. We did not find any observable evidence of a pileup happening in ObsID 0770580701. For ObsID 0770580901, we extracted source events from a circular region of radius 20″ about the source coordinates.

2.2. NuSTAR

The NuSTAR (Harrison et al. 2013) observations were processed through the NuSTAR Data Analysis Software (NuSTARDAS v1.8.0) and CALDB (v20190513). The light curves produced from the FPMA detector were gti- and barycenter-corrected using the `nuproducts` command. They were produced from the broad energy band of 3–79 keV at a binning of 0.07 s. The events were extracted from a circular region of 20″ centered on the target coordinates.

2.3. SWIFT

Following its detection by MAXI as MAXI J0051–736, Kennea et al. 2015 confirmed the outburst for SMC X-2 with a follow-up Swift ToO observation. For our investigation, we considered Swift/XRT (Burrows et al. 2005) windowed timing (WT) mode observations in the first couple of months of the outburst dating from 2015 September 24 to 2015 December 15. Our products were processed using the standard `xrtpipeline` command. For the timing analysis of the light curves, we extracted the events using `xselect` from a circular region of radius of 47″, or 20 pixels about the source position, and we performed a barycenter correction on them following the recommendations suggested by the Swift/XRT team.[10] The background-subtracted spectra were generated using the Swift/XRT products generator tool[11] at the UK Swift Science Data Centre (Evans et al. 2007, 2009).

2.4. OGLE

Prior analysis of OGLE III data was performed by both Schmidtke et al. (2006) and Schurch et al. (2011). In the case of the latter, it was concluded definitely that the northern star shows periodic variability, as opposed to its southern counterpart. These authors were also able to constrain the ephemeris and an accurate orbital period for the system by studying a long baseline of 7 yr of data.

In our work, we analyzed the 10 yr (2010–2019) OGLE IV data (Udalski et al. 2015), looking for photometric variations during this time. We analyzed each individual year of data looking for periodicities by detrending the signal and applying the Lomb–Scargle periodogram (Lomb 1976; Scargle 1982) technique to it. The detrending was done to remove large aperiodic variations and improve sensitivity to detect smaller periodic signals for the optical light curves.

3. Analysis and Results

3.1. Modeling with Polestar

3.1.1. The Fitting Procedure

Polestar (Cappallo et al. 2017) is a vector-based, physical model of an XRP. It contains parameters that represent the locations of two magnetic hot spots on the NS surface in an antipodal arrangement, along with both pencil- and fan-beam emission beaming functions. After applying a gravitational light-bending approximation (Beloborodov 2002), a model pulse profile is produced that can be fit to observed pulse profiles in order to suggest a likely geometry and orientation of a given XRP. The six free parameters of Polestar are as follows: the inclination angle of the spin axis with respect to the observer's line of sight ($0^\circ \leqslant i \leqslant 90^\circ$), the inclination angle of the magnetic dipole axis with respect to the spin axis ($0^\circ \leqslant \theta \leqslant 90^\circ$), the longitude (i.e., phase, $0^\circ \leqslant \phi \leqslant 360^\circ$), the exponent of the pencil-beam function ($1 \leqslant P_{\cos} \leqslant 4$), the exponent of the fan-beam function ($1 \leqslant P_{\sin} \leqslant 4$), and the relative contribution of each beaming function to the overall emission ($0 \leqslant P_{\rm rat} \leqslant 1$).

In this analysis, all parameters were allowed to freely vary within their respective ranges. Based on the statistical results from this blind fit, the mean inclination angle i was determined, along with the associated standard deviation of the resulting distribution (σ_i).

3.1.2. Fitting the Profiles

The Swift/XRT observations have lower sensitivity and shorter exposures in comparison to the XMM-Newton and NuSTAR observations. This led to better count statistics in the XMM-Newton and NuSTAR profiles, which were used in the Polestar modeling. In this work, all pulse profiles were created from their respective instrument's broad energy ranges (XMM-Newton at 0.2–12 keV and NuSTAR at 3–79 keV) in order to maximize the source signal-to-noise ratio.

Out of the six NuSTAR and XMM-Newton profiles, we chose to fit the pulse profiles from the observations belonging to the high flux states for better count statistics, setting a flux threshold. The ObsIDs 90101017002 and 0770580901 were disregarded for our fitting exercise. The profiles fitted with Polestar are given in Figure 2.

We folded the profiles for the remaining observations at their respective frequencies and frequency derivatives using the `efsearch` tool from the `HENDRICS` (Bachetti 2015) script within a targeted frequency range.

The resultant mean inclination angle came out to be $87^\circ \pm 4^\circ$ from the fitting exercise. The results are shown in Table 1.

[7] http://nxsa.esac.esa.int/nxsa-web
[8] https://www.cosmos.esa.int/web/xmm-newton/sas-thread-epic-filterbackground
[9] https://heasarc.gsfc.nasa.gov/docs/xmm/abc/node10.html
[10] https://www.swift.ac.uk/analysis/xrt/
[11] https://www.swift.ac.uk/user_objects/index.php

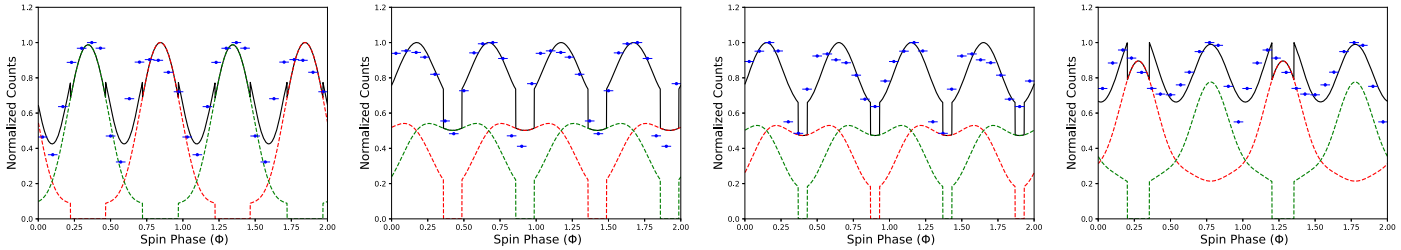


Figure 2. Profiles fitted with Polestar. The data points are represented in blue, while the black solid line is the total emission contribution from the model. The red and green dashed lines represent the contributions from the individual hot spots. (a) ObsID 90102014002, (b) ObsID 0770580701, (c) ObsID 0770580801, (d) ObsID 90102014004.

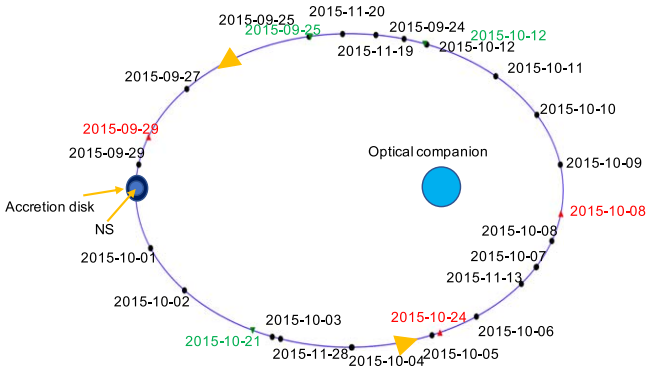


Figure 3. Schematic diagram (not to scale) of the SMC X-2 system. The various points indicate the approximate NS positions when the observations were made by the different telescopes during the 2015 outburst. Only observations with pulsations ($s > 90\%$) are shown. The black circles represent Swift, while red and green triangles denote XMM-Newton and NuSTAR, respectively. The NS in the figure is situated at apastron. The ephemeris is adopted from Schurch et al. (2011). The Swift data are summarized in Table 2. The majority of the Swift observations (not all) are marked in the figure with their dates of observation.

The XMM-Newton and NuSTAR profiles used in our fitting exercise were all double-peaked, with the two peaks having a separation of roughly a quarter of a phase. This appears to be a common feature of this source when in high luminosity states, as the two peaks were also observed in the outburst of 2000.

3.2. Source States

During its giant outburst in 2015, SMC X-2 was monitored by multiple observatories, providing good coverage of the flux variability throughout the outburst. Figure 3 depicts the positions of SMC X-2 in its orbit at the time of the observations by Swift, XMM-Newton, and NuSTAR. The evolution of the spectral state of any compact object during an outburst can be traced on a hardness intensity diagram (HID). Different sources proceed along different paths in their HID, determined by their natures. For example, in the case of black hole X-ray binaries (BHXBs), there is a common q-shaped trajectory (Homan & Belloni 2005; Remillard & McClintock 2006; Belloni 2010). For NS X-ray binaries, there are two different branches, known as horizontal and diagonal (Reig et al. 2006; Reig 2008). These branches are correlated with two types of distinct spectral states. The diagonal branch represents a high luminosity, spectrally soft state, while the horizontal branch indicates a low luminosity, spectrally hard state. The progression of a source along these two branches is influenced by accretion mechanism transitions. A change in accretion column height in conjunction with photon scattering

Table 1
Results of the Polestar Fitting of the Four Profiles under Consideration

ObsID	i	θ	ϕ	$P_{\cos}$	$P_{\sin}$	$P_{\rm rat}$
90102014002	80.0	88.0	56.0	2.5	1.0	0.9
0770580701	90.0	50.0	28.0	1.0	2.5	0.5
0770580801	90.0	46.0	216.0	1.0	3.5	0.5
90102014004	86.0	48.0	260.0	3.5	1.5	0.8

Note. The columns are as follows: observation ID, inclination angle between the line of sight and spin axis (i), angle between the magnetic dipole axis and spin axis (θ), phase (ϕ), power of the cosine beaming function ($P_{\cos}$), power of the sine beaming function ($P_{\sin}$), and ratio between the cosine and sine beaming functions ($P_{\rm rat}$). The mean inclination angle is $87^\circ \pm 4^\circ$, where the uncertainty is represented by the standard deviation of the distribution.

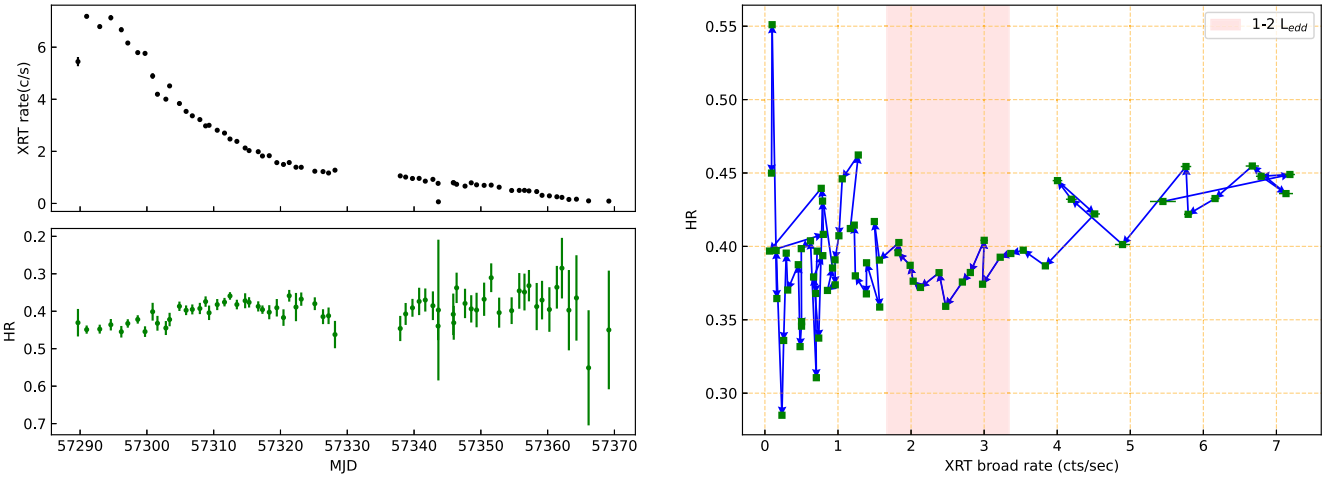
inside the column will result in a change of hardness ratio (HR) and thus movement in the HID. The HIDs are well equipped to reflect the spectral variations in the X-ray band, as the count rates are calculated from the same instrument. Additionally, the two branches are indicative of two different accretion regimes, subcritical and supercritical (Becker et al. 2012). These regimes are divided by the critical luminosity ($L_{\rm crit}$).

We calculated the HRs for SMC X-2 throughout the 2015 outburst for the majority of the Swift/XRT observations in the following energy ranges: 1–2 and 2–10 keV. The broad rate is taken from the energy range of 0.5–10.0 keV. The background-subtracted count rates in the different bands were obtained from the Swift/XRT product generator tool. In this analysis, we define the HR as

$$\mathrm{HR} = \frac{\mathrm{H} - \mathrm{S}}{\mathrm{H} + \mathrm{S}}, \tag{1}$$

where H and S are the count rates in the hard and soft spectral bands, respectively. The count rate fluctuation in conjunction with the simultaneous evolution of the HR is presented in Figure 4(a). While the count rate diminished consistently after the outburst, the HR remained relatively constant at values around 0.4. This indicates that the source remained in the hard state for almost the entirety of the outburst with very little variation and no observable evidence of hysteresis.

The evolution of the HR is presented in Figure 4(b), with blue directional arrows depicting the observations in chronological order. We find that the source at the onset of the outburst starts from a relatively hard state with a count rate varying between ~5 and 7 counts s^{-1} and then descends toward a softer state within the shaded region (i.e., a factor of 1–2 greater than the Eddington limit). To estimate the count rate to flux conversion factor, we



(a) (b)

Figure 4. (a) The top panel displays the Swift/XRT count rate evolution during the 2015 outburst; the corresponding HR values are in the bottom panel. The HR is calculated using Equation (1) for the soft 1–2 keV and hard 2–10 keV bands. (b) The HR vs. count rate in the broad 0.5–10 keV band. The blue arrows are included to depict the flow of time and connect observations in chronological order. The shaded region indicates count rates between one and two times the Eddington luminosity.

calculated the values from the Swift spectral fits of the source during its high- and low-flux states using the model described in Section 3.3. We found comparable values and settled on an average of 9.1×10^{-11} erg cm^{-2} count^{-1}. Below the Eddington level, the source variability starts moving back and forth along the horizontal branch of the HID.

Results from Reig (2008) and Reig & Nespoli (2013) showed that some Be X-ray binaries, such as 4U 0115+63, KS 1947 +300, EXO 2030+375, and V0332+53, displayed horizontal as well as as diagonal branches in their respective HIDs. The data in the aforementioned works were taken from RXTE PCA light curves. All of these pulsars underwent type II outbursts, leading to their journey along the branches of the HIDs.

3.3. Pulsed Fraction Reversal

We also examined the pulsed fraction (PF) evolution of SMC X-2 in conjunction with X-ray luminosity. The Swift observations were considered for this, as they extended ∼80 days into the outburst, providing a wide temporal window to investigate the changes in the emission mechanism of the source.

The Swift spectra were grouped to have at least one count per bin, which suggested the use of the Cash statistic (Cash 1979) to fit the spectra. All energies below 0.7 keV were ignored to avoid "bump"-like features in the spectra at low energies.[12] The spectra were fitted using a simple power law with an associated absorption component through the model `phabs` (phabs*po) in XSPEC version 12.11.0 (Arnaud 1996). In this analysis, the unabsorbed flux was calculated for the energy range 0.5–10 keV (Table 2). This model was also applied by Lutovinov et al. (2017) to depict the evolution of the bolometric flux of the source in the 0.5–100 keV range during the 2015 episode. The unabsorbed luminosities were calculated assuming a distance of 62.44 kpc to the SMC (Graczyk et al. 2020).

For measuring the PF, we used the rms definition,

$$PF_{\rm rms} = \frac{\sqrt{2}\,F_{\rm rms}}{F_{\rm mean}}, \qquad (2)$$

[12] https://www.swift.ac.uk/analysis/xrt/digest_cal.php

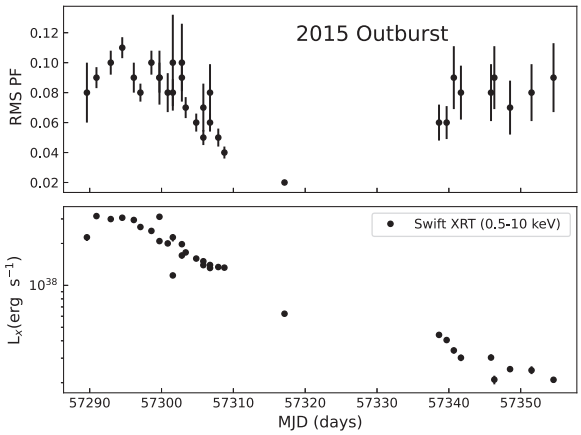


Figure 5. The PF and corresponding luminosity evolution of SMC X-2. We consider the unabsorbed fluxes here. Only the ObsIDs with pulsations at a significance >90% are reported here. Details of the corresponding ObsIDs are listed in Table 2.

where $F_{\rm rms}$ is the rms flux value, and $F_{\rm mean}$ is the mean flux. For sinusoidal profiles, the pulsed flux component $F_{\rm pulsed} = \sqrt{2}$ $F_{\rm rms}$ (Bildsten et al. 1997). In the following analysis, we use counts/count rates from the binned profiles as opposed to flux values.

During the early phase of the outburst (Figure 5), the pulse profiles were double-peaked, as they remained throughout the peak of the outburst and for ∼30 days after. As the X-ray luminosity declined, the Swift profiles transitioned from double- to single-peaked, with the transition occurring around MJD 57317. Then, after a period of not detecting significant pulsations, we again detected pulsations in the later phase of the outburst. At this point, the pulse profiles were single-peaked.

The evolution of the PF during this outburst is presented in the upper panel of Figure 5. Initially, the PF increased in conjunction with a rising X-ray luminosity. This correlation with $L_{\rm X}$ continued throughout the double-peaked phase of the outburst; as the luminosity declined, so did the PF. When the

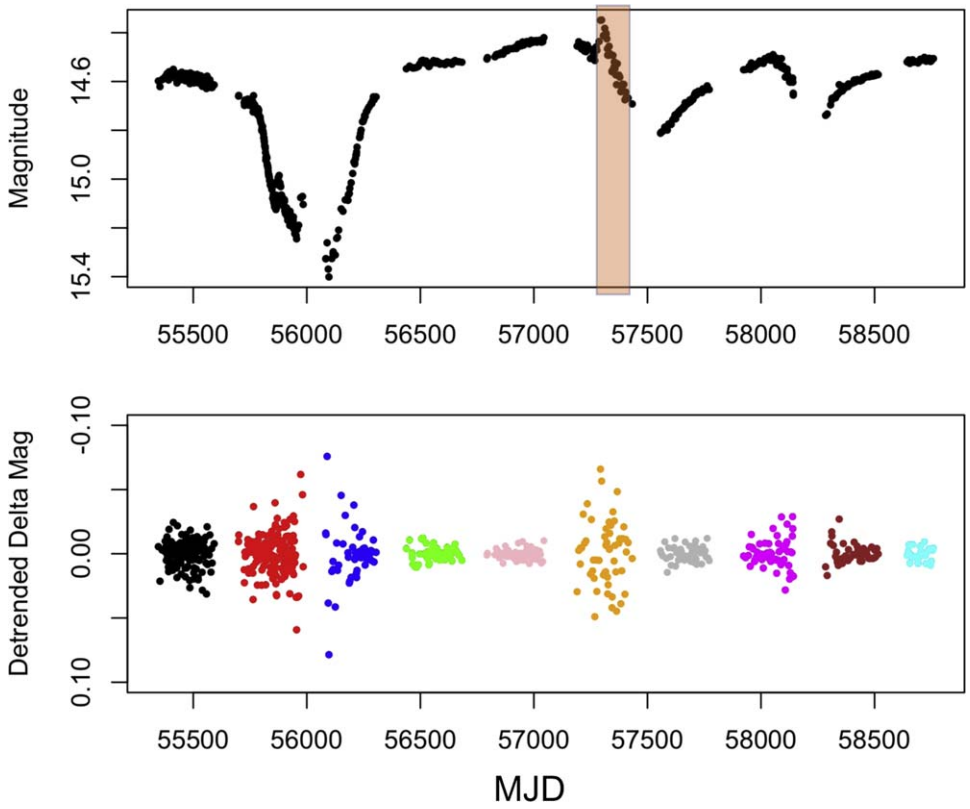


Figure 6. Top: OGLE IV optical light curve for the optical counterpart of SMC X-2. The type II outburst happened during the OGLE IV monitoring, as shown by the shaded region. Bottom: detrended light curve for each individual year.

pulsations reappeared with the single-peaked profile structure, the PF became anticorrelated with L_X, with the PF rising as SMC X-2's luminosity declined throughout the final weeks of the Swift monitoring data.

3.4. Analysis of the Light Curve of the Optical Companion

3.4.1. Previous OGLE III Analysis

On analyzing the 5 yr photometry data of OGLE III, Schmidtke et al. (2006) found weak periodic signals at 23 and 46 days, but they attributed those to aliasing, as the folded light curves showed little sinusoidal variation. They suggested that the northern star was the more likely counterpart, since it showed a variation over a range of ∼1 mag, as opposed to the small photometric variation observed in the light curve of the southern star. Later, McBride et al. (2008) determined the spectral classification of the star to be O9.5 III-Ve. The orbital period measurement of the star was first made by Schurch et al. (2011), who found a strong periodic signal corresponding to 18.62 ± 0.02 days in the combined last 4 yr of the OGLE III run, along with harmonics at 9.31 and 6.21 days. They solidified the northern star as the true optical counterpart in the SMC X-2 system, since the optical light curve for the southern star did not yield any periodic signatures. Though Schmidtke et al. (2009) proposed that the 18 day periodic signal is an artifact of the 9 and 6 day harmonics, Schurch et al. (2011) showed orbital modulation corresponding to the 18.62 day X-ray orbital period.

Schurch et al. (2011) showed that the orbital modulation of the source (see their Figure 4) is driven by the increase of accretion rates as the NS approaches the optical companion leading up to periastron. The folded optical light curve at $P_{orb} = 18.62$ days showed a sharp peak with an additional weak emission peak at 0.65 phase. Townsend et al. (2011) refined the period by fitting the pulse periods determined from the RXTE observations in 2000 to 18.38 ± 0.02 days. Similar pulse period fitting efforts by La Palombara et al. (2016) and Li et al. (2016) on Swift/XRT data from the 2015 outburst yielded consistent orbital periods of 18.38 ± 0.96 and 18.33 ± 0.17 days, respectively. Among the different methods discussed above, the most reliable method for orbital period determination is from Doppler modulation of pulse period measurements, providing a good estimate for the binary orbit of the NS.

3.4.2. OGLE IV Light Curve Analysis

In the following analysis, we searched for periodic signals in the OGLE IV data set. The OGLE IV database for SMC X-2 in this study extended across ∼a decade, from 2010 to 2019. The optical companion is listed as SMC 720.17 50 in the OGLE IV (Udalski et al. 2015) catalog.

The *I*-band light curves corresponding to each year were detrended with a Savitzky–Golay filter (Savitzky & Golay 1964) using a second-order polynomial. Similar applications of frequency filtering have been used in previous studies (Bird et al. 2012; Sturm et al. 2014). As in Treiber et al. (2021), the window length was kept larger than the orbital period to ensure no unintended influence on the shape of the profile. The top panel of Figure 6 shows the optical modulation during the OGLE IV monitoring and its corresponding detrended curves. The sharp spike in the highlighted region indicates the peak of the outburst. The strongest optical modulation is found in the third and sixth years of

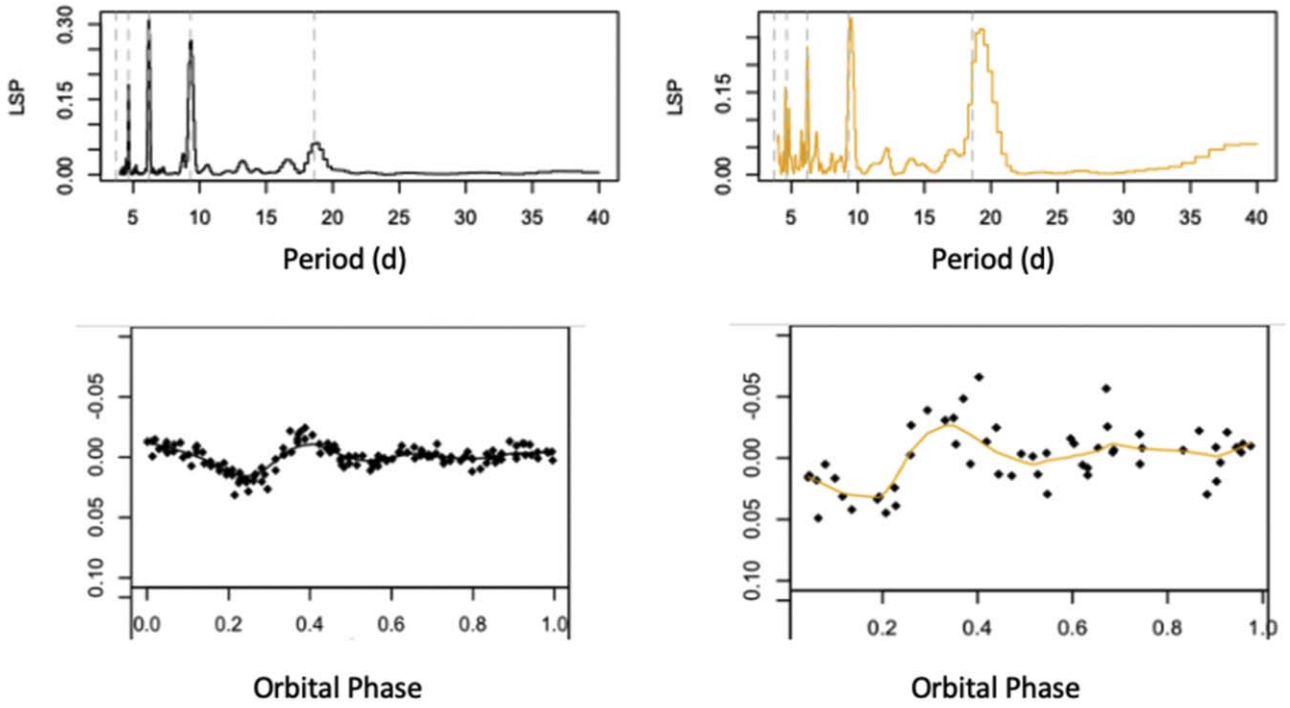


Figure 7. Top: Lomb–Scargle periodogram of the detrended light curve from the first (left) and sixth (right) years of the OGLE IV run. Bottom: optical profiles of the respective year light curves folded at 18.62 days. The dashed lines represent the harmonics belonging to the 18.62 day modulation proposed by Schurch et al. (2011) for OGLE III.

observations, the latter coinciding with the 2015 outburst (bottom panel of Figure 6).

On folding the detrended light curves on the known ephemeris of the source ($P = 18.62$, $T_{\rm per} =$ MJD 53170.7; Schurch et al. 2011), we find two maxima occurring at phases 0.0 (assumed to be the periastron) and 0.35, separated by a deep minimum. In the sixth-year folded profile (Figure 7), the stronger peak at the 0.35 phase approximately coincides with the time when the X-ray flux reached maximum (MJD 57290–57295), considering phase 0.0 as the pericenter point.

Lomb–Scargle periodogram analysis was performed on each year of the OGLE IV optical curve by first plotting the expected harmonics ($n = 1$–4) from Schurch et al. (2011) and then calculating the period and power of each peak corresponding to a given harmonic. On estimating the average, weighted by spectral power, we propose a period of $P = 18.74 \pm 0.39$ days, which is consistent with the period suggested by Schurch et al. (2011) within the uncertainties. The slight shift from the previously reported orbital period may be indicative of a distortion within or a precession of the Be disk.

4. Discussion

The 2015 type II outburst of SMC X-2 spanned a period of almost 3 months and reached X-ray luminosities that exceeded the Eddington limit. Figure 3 shows the approximate positions of the NS with respect to the optical star at the different points of observation as seen by XMM-Newton, NuSTAR, and Swift. The periastron point was determined from the ephemeris of the source (Schurch et al. 2011) during the epoch of maximum optical brightness. The first observation by Swift happened on 2015 September 24. The whole episode lasted for more than one orbital period, as is evident from the temporal distribution of the points on the orbit.

Some of the key findings and inferences that can be drawn from our analysis are discussed below.

4.1. Geometrical Modeling

Our modeling effort with Polestar aimed to determine the geometrical orientation of the pulsar by using a pulse profile–fitting algorithm comprised of emission beam parameters along with general relativistic approximations for light bending due to the NS's immense gravity.

On applying the model to the XMM-Newton and NuSTAR profiles, we were able to constrain the approximate geometry of the pulsar to the inclination angle of the spin axis, $i = 87^\circ \pm 4^\circ$ (Table 1). For the magnetic dipole inclination angle, we suggest that the most probable inclination is $\leqslant 50^\circ$. The X-ray data for the XMM-Newton and NuSTAR observations are summarized in Table 3.

Pulse profiles exhibiting dominant fan-beam emission have eclipse like cutoffs present in them (Wang & Welter 1981). Similar distinct features can be seen in the profiles previously fitted with Polestar from antipodal hot spots (Cappallo et al. 2019; Figures 2(b) and (c)). In their analysis of the pulse profile evolution of V0332+53, Sasaki et al. (2012) studied a similar transition, suggesting an oscillation from an accretion mound to a column and back to a mound throughout the duration of the outburst. The formation of the mound takes place in the initial stages of accretion when the mass accretion rate is relatively low. Gradually, with more mass inflow from the optical counterpart onto the NS, photons are emitted perpendicular to the accretion column walls, leading to fan-type emission (Postnov et al. 2015).

In Figure 2(a), there is no sharp dip, indicating a stronger pencil-beam contribution. The luminosity for this NuSTAR observation in the 3–70 keV band is measured to be 5.5×10^{38}

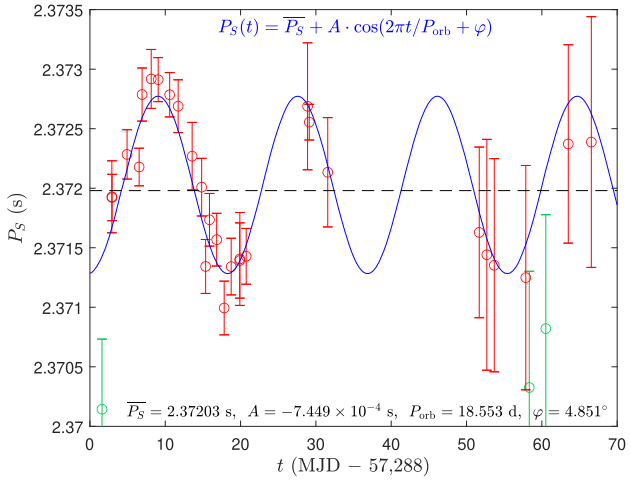


Figure 8. Sinusoidal fit to the measured spin periods (open circles) of the pulsar SMC X-2. The best-fit curve shows an average spin period of $\overline{P_S} = 2.37203(4)$ s and a binary orbital period of $P_{\rm orb} = (18.553 \pm 0.223)$ days. Deviations of measurements from the sinusoidal curve likely represent actual changes in P_S due to intermittent accretion events, in which case, they can reveal the movements of the magnetosphere against the inner edge of the accretion disk. The green points indicate the outlier points.

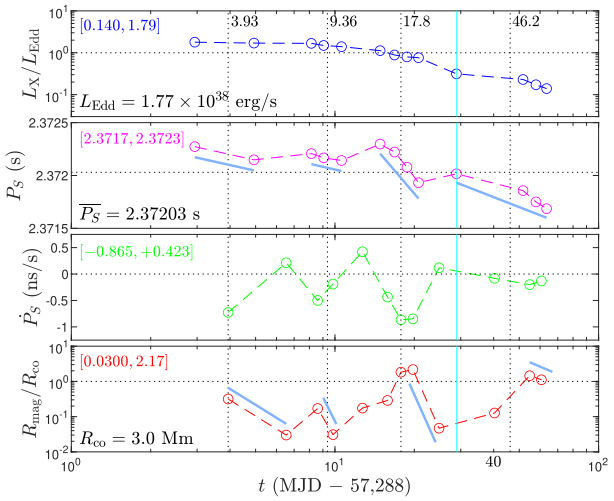


Figure 9. Time evolution past maximum of the X-ray luminosity L_X, the spin period P_S and its first-order numerical time derivative $\dot{P}_S$, and the magnetospheric radius $R_{\rm mag}$ of the SMC X-2 pulsar during its 2015 outburst and subsequent return to quiescence. Short-term fluctuations in L_X and P_S have been suppressed, and the periodic modulation due to orbital motion (Figure 8) has been removed from the P_S values. Ranges of variables are shown in square brackets. Four spin-up episodes are highlighted by tilted solid-line segments in the P_S and $R_{\rm mag}$ diagrams. The four corresponding vertical dotted lines indicate the times t at the midpoints of these spin-up episodes. The vertical solid line shows the onset of the subcritical accretion regime into which the pulsar crossed on day 29, if not a few days earlier (Figure 10 and footnote 8 below). The propagation of the uncertainties to obtain estimates of the error bars in magnetospheric movements is summarized in Appendix D.

erg s^{-1} (Jaisawal & Naik 2016). Using the relation for luminosity of an accreting NS to its mass accretion rate $\dot{M}$ (Sibgatullin & Sunyaev 2000), we estimate that $\dot{M}$ for this lies in the fan beam dominated ranges (Basko & Sunyaev 1976). Paul et al. (1997) also noticed the presence of pencil-beam patterns in the double-peaked profiles of GX 1+4 at high luminosities. The presence of the pencil-beam features in our pulse profile may be a result of the secondary polar beam reflected off the NS atmosphere (Wang & Frank 1981; Trümper et al. 2013). The combination of the fan beam directed perpendicular to the dipole axis and the polar beam directed along the magnetic axis may result in the pencil beam like features occurring in the beam patterns. Koliopanos & Vasilopoulos (2018) also suggested a similar phenomenon happening for SMC X-3, which underwent a similar large outburst in 2016.

4.2. Evolution of the Emission Pattern

Seminal studies on the HIDs of high-mass X-ray binaries (HMXBs) by Reig (2008) and Reig & Nespoli (2013) have given us a perspective on the evolution of the HR during an outburst for these systems.

In Section 3.2, we discussed our findings regarding the progression of the source states during the outburst. In Figure 4(b), a slight softening is seen as the luminosity starts to fall after the start of the outburst. This branch begins well above the Eddington luminosity level and then starts to meander below the Eddington level to form what is possibly the horizontal branch, according to Reig & Nespoli (2013).

A diagonal branch may be located within the highlighted region in Figure 4(b) corresponding to 1–2 $L_{\rm Edd}$, a feature in common with the HIDs studied by Reig (2008). The hardening above this branch has also been seen for other sources, such as SMC X-3 (Koliopanos & Vasilopoulos 2018) and RX J0209.6–7427 (Vasilopoulos et al. 2020), during their respective outbursts in 2016 and 2019. This branch has not been detected in the case of the HMXBs studied by Reig & Nespoli (2013). A plausible reason for this can be that the sources from that work never reached Eddington level luminosities. As suggested in Vasilopoulos et al. (2020), the hardening of the spectral states with luminosity can be attributed to specific changes in the accretion column, for instance, a change in the height or width of the base. Stabilization of the HRs at these levels can be a result of the physical limitations of the accretion column itself. Interestingly, such a variation is not uncommon within the pulse phase (see Figure 5 of Vasilopoulos et al. 2020) and is linked to the anisotropic emission behavior of XRPs, which is a contributing factor to the fan-beam emission.

Furthermore, the critical luminosity of the source that separates the supercritical from the subcritical accretion regime (Becker et al. 2012) was constrained by our analysis, and we found that this threshold is very much related to the observed reversal of the PF discussed in the next subsection. We describe these results in Appendix B.

4.3. PF Evolution

The evolution of the PF from the Swift observations is shown in Figure 5.

In our analysis, we considered Swift data points for which our Lomb–Scargle analysis yielded pulsations at significance (s) >90%. We used a finite interval about the fundamental and first harmonic of the spin period to perform the search for periods. We find that the PF decreases along with luminosity in the first half of the outburst extending up to 30 days from the first observation. In the later phase, when the luminosity starts to decline further, a nominal increase in the PF is observed.

Yang et al. (2018) conducted a long-term study of the anticorrelation behavior of the PF with luminosity in the case of SXP 1323 using XMM-Newton and Chandra observations. A

possible reason for this behavior has been explained due to spherical accretion. With an increase in luminosity, spherical accretion onto the compact object increases, leading to the production of soft thermal photons (due to the heating up of the NS atmosphere). These soft photons are responsible for more unpulsed flux components as compared to the pulsed flux contribution from the emission hot spots. Here the authors also cited examples where the PF increased with decreasing energies for the case of V0332+53 (Tsygankov et al. 2010), where they noticed an anticorrelation and a positive correlation at lower and higher luminosities, respectively, similar to SMC X-2.

Koliopanos & Vasilopoulos (2018) found an interesting evolution for SMC X-3 where the PF increased at lower count rates with a corresponding increase in pencil-beam radiation where $F_{\rm polar}/F_{\rm fan} > 2$ (here the ratio defines the relative intensities of the polar and fan beams). In this regime, the emission pattern was mostly of the pencil-beam type, while at higher count rates, the fan beam starts getting stronger. However, they did not report a steady increase in the PF at higher luminosities, suggesting that the reflected fan-beam radiation or the polar beam still plays a considerable role at higher mass accretion rates. This indicates the saturation of the accretion column height in the supercritical regime (Mushtukov et al. 2015).

4.4. Movements of the Magnetosphere of SMC X-2

During a large part of its decline toward the propeller line, SMC X-2 remained relatively bright, and this is why we were able to measure the spin period of the pulsar in several lower luminosity Swift/XRT observations. Here the propeller line refers to the lowest-level X-ray luminosity emitted when accretion is minimal. The dimmest state (ObsID 00034073100) for which P_S was measured at 99% significance was characterized by an unabsorbed flux of $F_{\rm X,min} = 4.53 \times 10^{-11}$ erg s^{-1} cm^{-2} corresponding to $L_{\rm X,min} = 2.11 \times 10^{37}$ erg s^{-1}, a factor of 15 below the maximum observed luminosity (and a factor of only 6 above the propeller line; Appendix C).

The coverage in P_S extends to ~80 days past maximum (as we describe in Appendix C, on day 84, the pulsar abruptly dropped down to the bottom of the Corbet gap). This coverage is sufficient for an in-depth study of the physical changes that were taking place in the tug-of-war between the magnetosphere and the accretion disk before the pulsar returned to quiescence. We took the following steps in our analysis.

1. Following the method of La Palombara et al. (2016), we determined the orbital modulation from the measured P_S values. In the process, four outliers indicating strong short-term fluctuations (large accretion-induced $\dot{P}_S$ values) were dropped from the data set. Then, a constant+sinusoidal fit to the data showed that P_S varied periodically around a mean of $\overline{P_S} = 2.37203(4)$ s with a best-fit orbital period of $P_{\rm orb} = (18.553 \pm 0.223)$ days (Figure 8), consistent with the results of previous models (Townsend et al. 2011; La Palombara et al. 2016). Due to the very small orbit of eccentricity ~0.07 (Townsend et al. 2011), this sinusoidal fit to the spin periods can be justified.
2. We assumed that any deviations ΔP_S of the points from the best-fit curve in Figure 8 represent actual changes in P_S from the mean value due to accretion, and we obtained the detrended spin periods $P_S = \overline{P_S} + \Delta P_S$ and their first-order numerical time derivatives $\dot{P}_S$.
3. We eliminated more points in order to suppress strong short-term fluctuations in flux and the numerical values of $\dot{P}_S$. The remaining 13 data points are plotted in Figure 9. The general trend is that luminosities decrease smoothly past a plateau near maximum, and spin periods indicate four spinning-up episodes taking place as the luminosities continue to fade.
4. Finally, in order to better understand the time evolution of the pulsar past the point of maximum luminosity, we calculated the magnetospheric radius $R_{\rm mag}$ (Figure 9, bottom panel), which is also the radius of the inner edge of the disk $R_{\rm d}$ in the ongoing tug-of-war (Equation (8) in Kluzniak & Lasota 2015; Christodoulou et al. 2018a, Equation (7)).

We detect in Figure 9 four separate incidents during which the pulsar was spinning up ($\dot{P}_S < 0$) despite the smooth decline in luminosity. These are highlighted by the tilted solid-line segments in the P_S and $R_{\rm mag}$ diagrams. After the initial push of the disk inside of corotation ($R_{\rm mag} = 0.03R_{\rm co} = 90$ km, day 7), the magnetic field pushed back toward corotation ($R_{\rm mag} = 0.17R_{\rm co} = 510$ km, day 9), only to be beaten back by the inflow near maximum luminosity on day 10. Two more spin-up episodes occurred on days 15–21 ($R_{\rm mag} = 2.17R_{\rm co} \simeq 6500$ km, day 20) and past day 29, when the source was about to enter the subcritical accretion regime.

During that last spin-up episode, the magnetosphere had already pushed out to beyond corotation ($R_{\rm mag} > 1.11R_{\rm co}$ on days >54), presumably terminating for good the loading of its field lines in this outburst cycle. It is apparent that the final spin-up was not caused by gas inflow from the disk ($L_{\rm X} = 0.9L_{\rm crit}$ on day 51 and smoothly declining by another factor of ~2, and so did the mass inflow rate). Thus, we are seeing a delayed unloading of gas previously loaded onto the field lines; this gas was reaching the accretion column of the pulsar at a slow rate, contributing a pencil beam of radiation for 38 days (29–67 days) that was also responsible for the observed increase of the PF (Figure 5). We have seen the same type of delayed clearing of the field lines in a similar study of SXP 1062 (Christodoulou et al. 2018a), where we had to work with sparse evolutionary data from González-Galán et al. (2018), and we called the delay in clearing "hysteresis." Indeed, there is an apparent lag in Figure 9 between each spin-up episode and the corresponding expansion of the magnetosphere. This lag is the outcome of the contributions of $L_{\rm X}$, P_S, and $\dot{P}_S$ in the complex tug-of-war that occurs past maximum luminosity, since $R_{\rm mag} = R_{\rm d} \propto [\dot{P}_S/(L_{\rm X}P_S^2)]^2$. Writing this relation in a compact form helps in delineating the hysteretical behavior of the two actual agents of change, the NS and the disk:

$$R_{\rm mag} = R_{\rm d} = R_*\left(\frac{\dot{\mathcal{L}}_*}{\dot{\mathcal{L}}_{\rm d}}\right)^2, \tag{3}$$

where $\dot{\mathcal{L}}$ represents the rate of change of angular momentum. Here $\dot{\mathcal{L}}_* \propto \dot{P}_S/P_S^2$ and $\dot{\mathcal{L}}_{\rm d} \propto \dot{\mathcal{M}}$, where $\dot{\mathcal{M}}$ is the mass inflow rate at the inner edge of the disk. In SMC X-2,

$R_{co}/R_* = \Gamma = 299$, and Equation (3) takes the particular form

$$R_{mag} = R_{co}\left(\frac{\dot{\mathcal{L}}_*}{17.3\ \dot{\mathcal{L}}_d}\right)^2. \quad (4)$$

The above two equations essentially represent torque balance, but the torque from the disk is not transferred to the NS instantly. For this reason, although the disk torque $\propto \dot{\mathcal{M}} \propto L_X$, most of the energy is not released at the inner edge of the disk. Therefore, Equations (3) and (4) are not valid during loading of the field lines, where wavelength-dependent magnetic instabilities take time to operate efficiently (Meszaros 1992). Time (~3–6 days) is needed for loading and for loads of gas to descend to the accretion column, where they will pile up and cause the $\dot{\mathcal{L}}_*$ to change measurably. Similarly, the magnetosphere cannot expand instantly in response to a reduced disk $\dot{\mathcal{M}}$. A nonzero $\dot{\mathcal{L}}_*$ is also involved, and when $\dot{\mathcal{L}}_d$ drops to ~6% of $\dot{\mathcal{L}}_*$ in SMC X-2 (Equation (4)), the field expansion may reach out to near corotation (in ~3–8 days).

This behavior is seen in Figure 9 three times (on days 9, 18, and 55), until finally $\dot{\mathcal{M}}$ became subcritical ($\dot{\mathcal{M}} < \dot{\mathcal{M}}_{crit} = 5.3 \times 10^{17}$ g s^{-1}, derived from $L_{crit} = 4.9 \times 10^{37}$ erg s^{-1}); then, the magnetosphere expanded unimpeded to beyond corotation (on days 40–55). On the other end, $\dot{\mathcal{L}}_d$ was 33% of $\dot{\mathcal{L}}_*$ on day 7, when R_{mag} was at its minimum and $\dot{\mathcal{M}}$ at the inner edge of the disk was 3.4×10^{18} g s^{-1}, that is, ~six times larger than its critical value $\dot{\mathcal{M}}_{crit}$ (see also Figure 10 below).

The spin-up episodes and magnetospheric movements discussed above raise a host of complicated technical issues relating to the physical conditions that arise when SMC X-2 enters its subcritical accretion regime. These conditions concern the reversal of the PF, the low-mass accretion states occurring at low X-ray luminosities, and the variability of the X-ray emission from the pulsar. We defer the presentation of such details to Appendix B.

5. Conclusions

In conclusion, we report a most likely geometry of SMC X-2 with the inclination angle between the spin axis and the line of sight as $i = 87° \pm 4°$. We also observe a rise in pencil-beam emission as the outburst progressed, along with a marginal rise in the PF. A possible reason for this suggested in this work is the delayed loading of the materials from the field lines leading to a gradual spin-up and increase in PF. This delayed clearing of the lines can be explained as hysteresis, which was also observed in the magnetospheric movement of other pulsars like SXP 1062.

This work was funded by NASA ADAP grants NNX14-AF77G and 80NSSC18K0430. The authors would also like to thank UMass Lowell and LoCSST (Lowell Center for Space Science and Technology) for their constant support. G.V. acknowledges support by NASA grant Nos. 80NSSC20K1107, 80NSSC20K0803, and 80NSSC21K0213. The authors would also like to thank the Swift help desk, M. Brumback, and L. Townsend for their helpful discussions. OGLE data are available through the OGLE XROM online portal.[13]

Software: HENDRICS (Bachetti 2015), SAS (v17.0.0; Gabriel et al. 2004), XSPEC (v12.11.0; Arnaud 1996), Polestar (Cappallo et al. 2017).

Appendix A
X-Ray Data

Below are summarized the X-ray data for our observations.

Table 2
Swift/XRT Observations (WT) with Detected Pulsations

ObsID	Start Time	Period (s)	Exposure (ks)	Flux[a]/10^{-10} (erg s^{-1} cm^{-2})
00034073001	2015-09-24 14:33:10	2.3701 ± 0.0006	2.0	$4.78^{+0.21}_{-0.28}$
00034073002	2015-09-25 22:32:58	2.3719 ± 0.0002	1.7	$6.79^{+0.11}_{-0.11}$
00034073003	2015-09-27 22:18:58	2.3723 ± 0.0002	1.6	$6.46^{+0.04}_{-0.13}$
00034073005	2015-09-29 12:46:58	2.3722 ± 0.0002	1.8	$6.60^{+0.14}_{-0.11}$
00034073007	2015-10-01 03:16:57	2.3729 ± 0.0002	2.0	$6.36^{+0.13}_{-0.14}$
00034073008	2015-10-02 01:29:57	2.3729 ± 0.0002	1.9	$5.67^{+0.09}_{-0.09}$
00034073009	2015-10-03 14:10:58	2.3728 ± 0.0002	1.9	$5.31^{+0.07}_{-0.08}$
00034073010	2015-10-04 17:05:58	2.3727 ± 0.0002	1.8	$6.71^{+0.12}_{-0.15}$
00034073011	2015-10-05 20:32:41	2.3711 ± 0.0008	0.5	$4.32^{+0.15}_{-0.16}$
00034073012	2015-10-04 16:57:58	2.3732 ± 0.0009	0.4	$4.49^{+0.21}_{-0.16}$
00034073013	2015-10-06 13:36:58	2.3736 ± 0.0020	0.2	$4.78^{+0.26}_{-0.32}$
00034073014	2015-10-06 13:43:58	2.3723 ± 0.0003	1.6	$2.54^{+0.08}_{-0.07}$
00034073015	2015-10-07 19:54:59	2.3713 ± 0.0014	0.3	$3.54^{+0.15}_{-0.18}$
00034073016	2015-10-07 20:02:58	2.3720 ± 0.0002	1.8	$4.26^{+0.15}_{-0.10}$
00034073018	2015-10-08 08:43:58	2.3713 ± 0.0002	2.0	$3.72^{+0.10}_{-0.08}$
00034073020	2015-10-09 19:50:58	2.3716 ± 0.0002	2.0	$3.36^{+0.07}_{-0.05}$
00034073021	2015-10-10 19:43:57	2.3718 ± 0.0012	0.4	$3.02^{+0.12}_{-0.13}$
00034073022	2015-10-10 19:48:58	2.3710 ± 0.0002	2.0	$3.22^{+0.06}_{-0.05}$
00034073023	2015-10-11 18:00:58	2.3709 ± 0.0012	0.4	$2.88^{+0.14}_{-0.14}$
00034073024	2015-10-11 18:05:58	2.3713 ± 0.0002	2.0	$3.02^{+0.06}_{-0.06}$
00034073026	2015-10-13 17:55:58	2.3714 ± 0.0002	2.2	$2.89^{+0.05}_{-0.06}$
00081771002	2015-10-12 21:30:58	2.3714 ± 0.0003	1.5	$2.92^{+0.08}_{-0.06}$
00034073044	2015-10-22 02:53:57	2.3726 ± 0.0002	8.3	$1.35^{+0.01}_{-0.03}$
00034073070	2015-11-12 15:11:16	2.3749 ± 0.0010	1.7	$0.95^{+0.04}_{-0.03}$

Table 2
(Continued)

ObsID	Start Time	Period (s)	Exposure (ks)	Flux[a]/10^{-10} (erg s^{-1} cm^{-2})
00034073072	2015-11-13 16:30:58	2.3716 ± 0.0007	2.4	$0.87^{+0.03}_{-0.04}$
00034073074	2015-11-14 16:41:32	2.3714 ± 0.0010	1.8	$0.74^{+0.03}_{-0.04}$
00034073076	2015-11-15 16:25:21	2.3714 ± 0.0009	2.0	$0.65^{+0.03}_{-0.04}$
00034073082	2015-11-19 20:49:58	2.3712 ± 0.0009	2.0	$0.65^{+0.03}_{-0.02}$
00034073084	2015-11-20 07:54:58	2.3703 ± 0.0010	2.0	$0.45^{+0.03}_{-0.03}$
00034073088	2015-11-22 12:35:58	2.3708 ± 0.0010	2.0	$0.54^{+0.02}_{-0.02}$
00034073094	2015-11-25 12:12:57	2.3724 ± 0.0008	2.4	$0.53^{+0.04}_{-0.03}$
00034073100	2015-11-28 13:35:58	2.3724 ± 0.0011	2.2	$0.45^{+0.02}_{-0.02}$

Note.
[a] The fluxes are reported as unabsorbed fluxes in the 0.5–10 keV range. The errors on the fluxes are within the 1σ confidence range. These are the ObsIDs we got significant pulsations for.

Table 3
XMM-Newton and NuSTAR Observations

ObsID	Start Time	Period (s)	Telescope	Flux[a]/10^{-10} (erg s^{-1} cm^{-2})
90102014002	2015-09-25 21:51:08	2.3719 ± 0.0003	NuSTAR	$4.16^{+0.02}_{-0.02}$
0770580701	2015-09-29 22:12:49	2.3728 ± 0.0002	XMM	$5.13^{+0.01}_{-0.01}$
0770580801	2015-10-08 20:56:53	2.3717 ± 0.0002	XMM	$3.10^{+0.01}_{-0.01}$
90102014004	2015-10-12 21:41:08	2.3714 ± 0.0004	NuSTAR	$1.72^{+0.01}_{-0.01}$
90101017002	2015-10-21 21:31:08	2.3727 ± 0.0005	NuSTAR	$1.19^{+0.01}_{-0.01}$
0770580901	2015-10-24 13:48:30	2.3721 ± 0.0005	XMM	$1.29^{+0.00}_{-0.00}$

Note. The XMM-Newton EPIC-pn and NuSTAR FPMA observations of SMC X-2 during the 2015 outburst. The fluxes are reported as unabsorbed fluxes in the 0.5–10 keV range.

Appendix B
Physical Conditions in SMC X-2 during Subcritical Accretion

Here we address several technical details concerning the physical conditions that pertain to SMC X-2 when the NS continues to evolve, albeit by accreting the inflowing matter at very low rates (the so-called subcritical accretion regime; Becker et al. 2012). The discussion that follows relies on the results described in the main text and illustrated in Figure 9.

B.1. Maximally Compressed Magnetosphere

Knowing the size of the magnetosphere at maximum luminosity provides a fifth independent method for the determination of the surface dipolar magnetic field of the NS, but the hysteretical events make such estimates only approximate because the minimum $R_{\rm mag}$ and the maximum $L_{\rm X}$ do not occur at the same time. Using Equation (11) from Christodoulou et al. (2018a), we estimated some possible values of the surface dipolar magnetic field $B_{\rm dip}$ across the 8 day luminosity plateau seen in the top panel of Figure 9, and they suggest that, at most, $B_{\rm dip} \sim 1$ TG (not $\sim$3 TG, as determined by cyclotron absorption; Jaisawal & Naik 2016 and Appendix C below.)

B.2. Rate of Change of Flux in the Subcritical Regime

In this analysis, we went to considerable lengths in order to document and understand the uncommon appearance of the reversal in the PF. Surprising as it may be, the few points that exhibited this reversal are also singled out by the rate of change of flux (or luminosity) as the outburst is winding down. Unfortunately, this type of diagram is not usually plotted on linear scales, and the identification was not made until late in our study. In Figure 10 (in which we use linear axes[14]), a dramatic change in slope by a factor of $\sim$10 is evident in the approximately linear decrease of $L_{\rm X}(t)$. The steep decline seen above the critical accretion threshold ($L_{\rm X}/L_{\rm Edd} = 0.277$) is severely curtailed past day 29,[15] and the disk cannot be held responsible for such an abrupt (discontinuous) change. Instead, it is the magnetic field lines that regulate the final load of gas deeply into the subcritical accretion regime. This conclusion is obtained directly from the observations of fluxes, without the need for additional data modeling.

[13] http://ogle.astrouw.edu.pl/ogle4/xrom/xrom.html

[14] On a logarithmic $L_{\rm X}$ scale, one would be tempted to fit one straight line to the data past day 10 (MJD = 57,298), as can be seen in the top panel of Figure 9 (and the bottom panel of Figure 5).

[15] Day 29 is not merely "close enough" to a possible key day 40 that could be surmised from the intersection of the critical and best-fit lines in the subcritical regime seen in Figure 10. The value of $L_{\rm crit} = 4.9 \times 10^{37}$ erg s^{-1} was derived above from the corresponding equation of Becker et al. (2012) assuming a canonical NS, but SMC X-2 is not a canonical pulsar. Work in progress shows that $L_{\rm crit}$ is 40% higher in SMC X-2 (i.e., $L_{\rm crit} = 0.390 L_{\rm Edd}$), in which case Figure 10 implies that the pulsar entered the subcritical accretion regime on day 29, if not a few days earlier. This threshold is also supported by the sharp reduction in flux variability seen past day 29 in Figure 11.

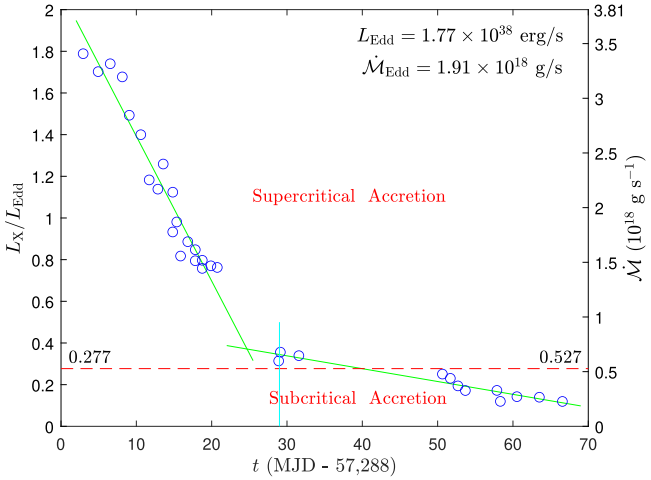


Figure 10. The X-ray luminosity L_X past maximum, scaled to $L_{\rm Edd}$, vs. time t during the 2015 outburst of SMC X-2. The solid lines are the best-fit lines in the two accretion regimes, with slopes of $(-6.95 \pm 0.40) \times 10^{-2}$ and $(-6.16 \pm 0.56) \times 10^{-3}$ day^{-1}, respectively. Below the critical accretion value of $L_{\rm crit} = 0.277 L_{\rm Edd}$, the luminosity declines ∼10 times slower than in the supercritical accretion regime. The axis on the right shows the corresponding mass accretion rates $\dot{\mathcal{M}}$ in units of 10^{18} g s^{-1}; the critical rate is 0.527 in these units. The vertical line segment marks day 29, when the pulsar crossed into the subcritical accretion regime.

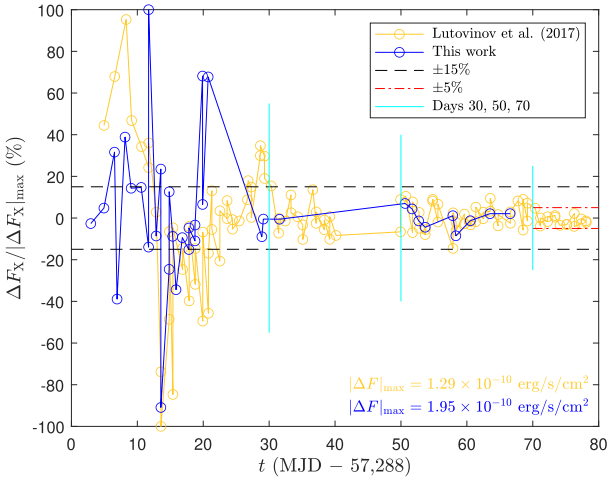


Figure 11. The X-ray flux variability ΔF_X, as a percentage of its absolutely maximum value $|\Delta F_X|_{\rm max}$, vs. time t past the luminosity maximum of the 2015 outburst of SMC X-2. The variability of the source dropped to <15% past day 30, when the mass accretion rate was only 10% higher than the critical value of $\dot{\mathcal{M}}_{\rm crit} = 5.3 \times 10^{17}$ g s^{-1}.

B.3. Conditions for Detecting PF Reversals

The onset of subcritical accretion does not automatically imply that an increase of the PF will be detected in X-ray observations over a period of several days. The final load of gas must also impart a substantial amount of angular momentum to the NS, as in SMC X-2 and SXP 1323 (Yang et al. 2018). If the dramatic change in slope did not occur in Figure 10, then the source would be cutting across and into quiescence without trapping a large load of gas between its field lines, as other HMXB sources appear to do (Coe et al. 2015). Such an additional condition may be discernible in the X-ray luminosities observed in the subcritical regime, which should be significant fractions of $L_{\rm crit}$ for PF reversal (PFR) to be observable. For SMC X-2, we found that the lowest luminosity with an increasing PF was $L_{\rm X,min} = 0.43 L_{\rm crit}$ (Swift ObsID 00034073100). For SXP 1323, only a rough estimate of its magnetic field is available (Christodoulou et al. 2018a), and it is surprisingly low ($B = 0.03$ TG). This estimate implies that the critical accretion luminosity is $L_{\rm crit} = 3.55 \times 10^{35}$ erg s^{-1} and the Coulomb-breaking luminosity is $L_{\rm coul} = 3.75 \times 10^{37}$ erg s^{-1} in SXP 1323 (so the accreted gas impacts the surface of the NS, as in Figure 1(a) of Becker et al. 2012, which reinforces the unusually weak magnetic field surmised for SXP 1323). The propeller state lies too low ($L_{\rm prop} = 1.44 \times 10^{27}$ erg s^{-1} for the current spin period of $P_S = 1100$ s) to play any role in the observations of SXP 1323. Yang et al. (2018) found that the lowest luminosity with a still increasing PF was $L_{\rm X,min} = 1.50 \times 10^{35}$ erg s^{-1} (XMM-Newton ObsID 135721901), which corresponds to $L_{\rm X,min} = 0.423 L_{\rm crit}$. The agreement between these two minimum values is quite encouraging, given all of the uncertainties confounding their estimates. With this limited information at our disposal, we determine that the subcritical range of X-ray luminosities,

$$(L_X)_{\rm PFR} \in [0.42, 1] \cdot L_{\rm crit}, \tag{B1}$$

is a necessary condition for PFR to be observable in HMXBs. The upper limit is set by the lack of strong variability past day 30 in SMC X-2 (see footnote 8 and Figure 11), thereby making it easier for PFR to be detected in the X-ray fluxes.

B.4. X-Ray Variability during the 2015 Type II Outburst of SMC X-2

Day 29 was also a threshold for severely diminished flux variability during the 2015 outburst of SMC X-2. Figure 11 shows day-to-day and intraday variability in the X-ray fluxes measured in this work and that of Lutovinov et al. (2017), respectively. As in Figure 10, line segments were fitted to the two accretion regimes in each data set, and they provided the baselines from which flux variations could be determined. For several days past maximum, the X-ray fluxes varied by as much as $1.86 F_{\rm crit} = 0.29 F_{\rm max}$ and $1.23 F_{\rm crit} = 0.20 F_{\rm max}$, respectively. Variability then decreased to <15% by day 29 and <5% by day 70. These large relative declines occurred as the mass accretion rate continued to decrease smoothly below the critical $\dot{\mathcal{M}}$ value at an average rate of $\ddot{\mathcal{M}} = -1.4 \times 10^{11}$ g s^{-2} (Figure 10). Thus, we conclude that these large reductions in X-ray variability do not signify an approach to the propeller state;[16] rather, they are a telltale sign of the pulsar having crossed into the subcritical accretion regime.

Appendix C
The Dipolar Magnetic Field of SMC X-2

Despite widespread agreement obtained by three different methods, the dipolar magnetic field of the pulsar remains uncertain. A cyclotron resonance absorption line found by Jaisawal & Naik (2016) at $E_{\rm cyc} \approx 27$ keV casts doubt on all other determinations if this value corresponds to the fundamental energy level ($n = 1$). For canonical pulsar parameters

[16] The propeller line of SMC X-2 ($L_{\rm prop} = 3.60$ erg s^{-1}; Appendix C) lies at an estimated X-ray flux of $F_{\rm prop} = 7.72 \times 10^{-12}$ erg s^{-1} cm^{-2}. The lowest-luminosity Swift observation (ObsID 00034073100), in which we detected a PFR, recorded a flux of $F_{\rm min} = 4.53 \times 10^{-11}$ erg s^{-1} cm^{-2} (Section B.3), about six times higher than the propeller line and more than twice lower than the critical (maximum) value for subcritical accretion.

and $n = 1$, we find from the equations given in Christodoulou et al. (2018c, 2019) that

$$B_{\rm cyc} = \left(\frac{E_{\rm cyc}}{8.86\ {\rm keV}}\right){\rm TG} \simeq 3.0\ {\rm TG}. \quad \text{(C1)}$$

Jaisawal & Naik (2016) called for $B = 2.3$ TG instead because they did not multiply by the correction term $(1 + z_{\rm g})$ due to gravitational redshift, which takes the canonical value of 1.306. In their study of the 2015 Swift/XRT data, Lutovinov et al. (2017) essentially corrected the discrepancy when they adopted the cyclotron value shown in Equation (C1).

The three different methods that point to a lower value of

$$B \simeq 1.2\ {\rm TG} \quad \text{(C2)}$$

are as follows.

1. The lowest X-ray luminosity for this source, $L_{\rm min} = 3.9 \times 10^{36}$ erg s^{-1}, was obtained by ASCA (Yokogawa et al. 2001, 2003). The prefactor in $L_{\rm min}$ is reduced to 3.6 for an SMC distance of 62.44 kpc (Graczyk et al. 2020), causing a minor change of 4% to the result. Identified with the propeller state (Illarionov & Sunyaev 1975), these $L_{\rm min}$ values imply that $B = 1.2$ TG (Christodoulou et al. 2018b) using the standard Equation (5) of Stella et al. (1986) with $P_S = 2.372$ s and canonical pulsar parameters, viz

$$L_{\rm prop} = 2 \times 10^{37}\left(\frac{B}{1\ {\rm TG}}\right)^2\left(\frac{P_S}{1\ {\rm s}}\right)^{-7/3}{\rm erg\ s^{-1}}. \quad \text{(C3)}$$

   The significance of this equation will be discussed below.
2. Four days after the last Swift/XRT detection (MJD 57371), an upper limit in the 0.5–10 keV flux was reported by Lutovinov et al. (2017) from a nearly 2 ks long exposure (ObsID 00034073135). The flux dropped abruptly by a factor of 200 to a value of $F_{\rm gap} \leqslant 3.0 \times 10^{-14}$ erg s^{-1} cm^{-2}, which led the authors to conclude that the source had transitioned to the bottom of the Corbet (1996) gap. Assuming this to be the case, we can rebuild the transition back up to the propeller state to obtain yet another independent estimate of the magnetic field.
   (a) *Bottom of the gap*.—At an SMC distance of 62.44 kpc, the observed upper limit implies an X-ray luminosity of $L_{\rm gap} = 1.4 \times 10^{34}$ erg s^{-1}.
   (b) *Gap factor* Γ.—The bottom of the Corbet (1996) gap lies below the propeller line by a factor of Γ, where $\Gamma = 168(P_S/1\ {\rm s})^{2/3}$ and $\Gamma = 299$ for $P_S = 2.372$ s.
   (c) *Propeller state*.—Using this value of Γ, we find a propeller state characterized by $F_{\rm prop} = \Gamma F_{\rm gap} = 9.0 \times 10^{-12}$ erg s^{-1} cm^{-2} and $L_{\rm prop} = \Gamma L_{\rm gap} = 4.2 \times 10^{36}$ erg s^{-1}.
   (d) *Magnetic field*.—Using this last value of the propeller luminosity in Equation (C3), we find that $B = 1.25$ TG on the propeller line.
   This method of determining the magnetic field has previously worked out well in millisecond binary pulsars, where the bottom of the Corbet (1996) gap can often be detected in X-rays (and the light cylinder too, in those pulsars with strong magnetic fields $B \sim 10^8$ G; Christodoulou et al. 2018c).
3. A clustering analysis of the propeller states of all Magellanic HMXB pulsars (Christodoulou et al. 2017, 2018b, 2019) placed SMC X-2 on the "third propeller line" ($B = (1.3 \pm 0.37)$ TG) above the absolutely lowest propeller line ($B = (0.28 \pm 0.08)$ TG). In support of this determination, a formal calculation of the cross-ratio of X-ray luminosity ratios $L_{\rm min}/L_{\rm max}$ between the two pairs of states at $P_S = 2.372$ s showed a "jump factor" of $J = 70$, implying that $B = 1.2$ TG (as listed in Table 3 of Christodoulou et al. 2017). The jump factor does not depend on whether emission is isotropic or beamed toward the observer.

C.1. Technical Remarks

Several remarks are in order here concerning various aspects and details of the calculations described above.

(a) An independent (fourth) calculation using the long-term (15 yr) spin period derivative ($\dot{P}_S = -1.4 \times 10^{-10}$ s s^{-1}; Yang et al. 2017) did not produce a similar value (the result was $B = 2.4^{+0.71}_{-1.0}$ TG; Christodoulou et al. 2018b), possibly because the error bar on $\dot{P}_S$ is too large (∼66%). It is worth noting that the cyclotron value (Equation (C1)) lies at the upper end of the error bar, whereas the value (Equation (C2)) determined by all other methods lies just below the lower end. These two values also accurately describe the fourth and third Magellanic propeller lines, respectively (Christodoulou et al. 2017, 2019). However, SMC X-2 cannot be associated with the fourth propeller line because the ASCA value of its $L_{\rm min}$ is too low, and its jump factor ($J = 70$) is lower than 100, which is roughly the lower cutoff of the fourth propeller line (see item (g) below).

(b) Christodoulou et al. (2018b) pointed out an agreement between the above $\dot{P}_S$-determined value of the magnetic field and the cyclotron value of 2.3 TG proposed by Jaisawal & Naik (2016). We now know that this agreement was entirely coincidental because $B_{\rm cyc}$ turns out to be 3.0 TG after $E_{\rm cyc}$ is corrected for gravitational redshift (Equation (C1)).

(c) The same redshift correction is missing from the fundamental equation for the critical luminosity $L_{\rm crit}$ separating pencil- and fan-beam radiation from an accretion column (Becker et al. 2012) that we use below to obtain more information related to the observed reversal of the PF in SMC X-2. Combining Equation (C1) with Equation (32) in Becker et al. (2012) and using canonical pulsar parameters, we find that

$$L_{\rm crit} = 1.70 \times 10^{37}\left(\frac{E_{\rm cyc}}{10\ {\rm keV}}\right)^{16/15}{\rm erg\ s^{-1}}, \quad \text{(C4)}$$

which corresponds to their Equation (55). For SMC X-2, $E_{\rm cyc} \approx 27$ keV, and this equation produces a threshold at $L_{\rm crit} = 4.9 \times 10^{37}$ erg s^{-1}. This value singles out the last few Swift/XRT observations at MJD − 57288 > 50 with unabsorbed fluxes $F_{\rm X} < F_{\rm crit} = 1.05 \times 10^{-10}$ erg s^{-1} cm^{-2} and corresponding luminosities $L_{\rm low} < L_{\rm crit}$ during which the PF reversed its monotonicity and no longer decreased with decreasing $L_{\rm low}$ values. All of these $L_{\rm low}$ values are larger by factors of 2.64–5.55 as compared to the Coulomb-breaking luminosity,

$$L_{\rm coul} = 1.12 \times 10^{37}\left(\frac{E_{\rm cyc}}{10\ {\rm keV}}\right)^{-1/3}{\rm erg\ s^{-1}}. \quad \text{(C5)}$$

For SMC X-2, $L_{\rm coul} = 8.0 \times 10^{36}$ erg s^{-1}. We find then that the PF reverses when the source enters the subcritical accretion

regime in which the final deceleration of the inflowing gas occurs at the base of the accretion column via strong Coulomb interactions. Although the magnetosphere has pushed out to beyond corotation (see Section 4.4), previously loaded gas is still reaching and piling up on the accretion column; SMC X-2 shows a temporary increase in the PF during this time-delayed accretion event, presumably the final event in this outburst cycle.

(d) Equation (C3) was derived by Stella et al. (1986) for the case of marginal accretion onto the magnetospheric lines of the compact object that occurs when the magnetospheric radius is equal to the corotation radius. This equation has worked very well, especially for HMXB sources with cyclotron resonance absorption lines in their spectra (Christodoulou et al. 2018c, 2019). (The only cyclotron cases shrouded with mystery and uncertainty are SMC X-2 and LXP 8.04.) Despite its successes, some researchers sought to modify the equation in ways that usually produce larger estimates for the dipolar magnetic fields (e.g., Campana et al. 2002, 2018; Tsygankov et al. 2016b, 2017; Fürst et al. 2017; Lutovinov et al. 2017; Vasilopoulos et al. 2018). Without getting into the technical details that are still being debated, we point out that such efforts are self-defeating because they introduce free parameters to the equations that may then be adjusted to drive the results to any desired outcome. For this reason, the importance of Equation (C3) as a "zeroth-order" result with no adjustable parameters is unquestionable, and its results have found support in several studies of HMXBs with and without cyclotron absorption lines (Klus et al. 2014; Christodoulou et al. 2017, 2018c, 2019; Tsygankov et al. 2017; Vasilopoulos et al. 2017, 2020; Maitra et al. 2018; Treiber et al. 2021).

(e) Campana et al. (2002), in their study of two well-known Galactic sources (4U 0115+63 and V0332+53), did not determine the propeller lines of the pulsars. They introduced a modified equation with an adjustable magnetospheric radius parameter ξ in place of Equation (C3), and they determined a range of $L_{\rm prop}$ values for $\xi \in [0.5, 1]$ using the known $B_{\rm cyc}$ values from cyclotron lines.[17] Tsygankov et al. (2016a) empirically determined the $L_{\rm prop}$ values from the same observations, but these values did not reproduce the known $B_{\rm cyc}$ values. These issues were resolved by calculations such as those described in method (2) above (Christodoulou et al. 2018c). Returning to the adjustable Equation (1) given in Campana et al. (2002), we can then determine for which value of ξ this equation produces consistent results for the two Galactic sources. We find that

$$\xi = 0.826, \tag{C6}$$

a value that also produces $B = 1.2$ TG for SMC X-2 using the same Equation (1) as presented by Lutovinov et al. (2017).

(f) For SMC X-2, the corotation radius of the accreted material is $R_{\rm co} = \Gamma R_* = 3.0$ Mm using the canonical radius of the NS $R_* = 10$ km and the value of Γ found above. On the other hand, the radius of the light cylinder is $R_{\rm LC} = cP_S/(2\pi) = 47.7(P_S/1\ s)$ Mm $= 113$ Mm, a factor of 38 farther than the corotation radius. Just as for all other HMXBs, the light cylinder is too far out in the accretion disk of SMC X-2 to play any role, unlike in the case of millisecond binary pulsars. The transition from the bottom of the Corbet gap to the light cylinder has never been observed in HMXB pulsars in quiescence, which also indicates that the magnetic fields of these objects are not of magnetar strength, a fact that has been largely ignored by the proponents of extremely high HMXB magnetic fields reaching near or beyond the quantum limit $B_{\rm QL} = 44.14$ TG (Erber 1966; Wasserman & Shapiro 1983).

(g) The jump factor J in method (3) above is a new parameter that provides independent estimates of HMXB dipolar magnetic fields (Christodoulou et al. 2018b, 2019). The five propeller lines, from lowest to highest, are characterized by

1. $B = (0.28 \pm 0.08)$ TG, $J \sim 1$–2,
2. $B = (0.55 \pm 0.11)$ TG, $J \sim 4$–13,
3. $B = (1.3 \pm 0.37)$ TG, $J \sim 70$,
4. $B = (3.0 \pm 0.68)$ TG, $J \sim 115$–260, and
5. $B = (7.9 \pm 3.1)$ TG, $J \sim 70$–100.

The highest propeller line is also highly uncertain.

Very few accreting pulsars with observed cyclotron absorption lines seem to fall between these levels (Jaisawal & Naik 2016; Staubert et al. 2019; Christodoulou et al. 2019), and these are all candidates for having substantial nondipolar magnetic components near their surfaces. Such higher-order multipolar components of the surface magnetic fields of XRPs are currently under investigation.

Appendix D
Error Propagation to the Magnetospheric Radius Values

Since $R_{\rm mag} \propto [\dot{P}_S/(L_X P_S^2)]^2$, the standard error propagation results in the following relative error for the magnetospheric radius $R_{\rm mag}$, i.e., $\Delta R_{\rm mag}/R_{\rm mag}$:

$$\frac{\Delta R_{\rm mag}}{R_{\rm mag}} = 2\sqrt{\left(\frac{\Delta \dot{P}_S}{\dot{P}_S}\right)^2 + \left(\frac{\Delta L_X}{L_X}\right)^2 + 4\left(\frac{\Delta P_S}{P_S}\right)^2}. \tag{D1}$$

In Table 4, we list the relative errors that we determined for the input parameters L_X and P_S used to produce Figure 9 and those obtained for the numerical derivatives $\dot{P}_S$. The latter errors were

Table 4
Relative Errors Propagated to the Magnetospheric Radii Shown in Figure 9 for SMC X-2

ObsID	$\Delta \ln F_X$	$\Delta \ln L_X$	$\Delta \ln P_S$	$\Delta \ln \dot{P}_S$	$\Delta \ln R_{\rm mag}$
00034073002	1.66e-02	0.112	8.21e-05	5.81e-04	0.225
00034073003	2.06e-02	0.113	8.74e-05	4.55e-04	0.226
00034073007	2.27e-02	0.113	1.04e-04	4.66e-04	0.227
00034073008	1.64e-02	0.112	7.79e-05	4.40e-04	0.225
00034073009	1.60e-02	0.112	7.85e-05	4.39e-04	0.225
00034073016	3.61e-02	0.117	1.02e-04	4.66e-04	0.234
00034073020	2.09e-02	0.113	9.33e-05	4.75e-04	0.226
00034073024	2.14e-02	0.113	1.00e-04	4.78e-04	0.226
00034073026	2.19e-02	0.113	9.88e-05	5.86e-04	0.227
90101017002	7.47e-03	0.111	2.25e-04	8.26e-04	0.223
00034073072	4.47e-02	0.120	3.02e-04	1.08e-03	0.240
00034073082	5.22e-02	0.123	3.97e-04	1.23e-03	0.246
00034073094	6.84e-02	0.131	3.51e-04	1.30e-03	0.261

Note.—The errors $\Delta \ln L_X$ include ± 0.47 kpc for the mean distance to the SMC (Graczyk et al. 2020), plus an estimated ± 3 kpc for the depth of X-2 within the Cloud (Figure 6 in Scowcroft et al. 2016); so, the adopted total relative error to the distance D of X-2 is $\Delta \ln D \approx \pm 6\%$.

[17] Note that the two equations do not agree for $\xi = 1$. Also, the actual debated range is $\xi \in [0.5, 2]$ (Frank et al. 2002), but values of $\xi > 1$ are presently avoided; owing to the steep dependence of $L_{\rm prop} \propto \xi^{7/2}$, they tend to produce unphysically high values for the propeller state in cases where the magnetic field is known from cyclotron absorption lines.

computed from Monte Carlo simulations, in which we assumed a normal distribution of errors for each individual spin period.

The above input values produce the relative errors for the magnetospheric radii $R_{\rm mag}$ that are also listed in the last column of Table 4. We see that the largest relative uncertainty in magnetospheric radius is

$$\frac{\Delta R_{\rm mag}}{R_{\rm mag}} \simeq \pm 26\%, \tag{D2}$$

and it occurs for one of the dimmer Swift observations taken near the end of the 2015 outburst (ObsID 00034073094). The errors in $F_{\rm X}$ are small because the Swift/XRT data that we used in Figure 9 were all obtained during long exposures (longer than 1.6 ks), and these are the ones that we trusted the most in our analysis. The errors in P_S are also small because the spin periods were all measured to a very high level of significance (>99%). Given these error bars and the larger uncertainties calculated for the numerical $\dot{P}_S$ values and the $L_{\rm X}$ values (dominated by the error in the depth of the source to within the SMC), the errors propagated to the $R_{\rm mag}$ values appear to be reasonable. These uncertainties indicate that the approximate movements of the magnetosphere of SMC X-2 illustrated in Figure 9 are likely realistic; thus, the observed phenomenon of hysteresis is probably real.

ORCID iDs

Ankur Roy https://orcid.org/0000-0001-6068-203X
Rigel Cappallo https://orcid.org/0000-0003-0267-8432
Silas G. T. Laycock https://orcid.org/0000-0002-8427-0766
Dimitris M. Christodoulou https://orcid.org/0000-0002-7652-2206
Georgios Vasilopoulos https://orcid.org/0000-0003-3902-3915
Sayantan Bhattacharya https://orcid.org/0000-0001-8572-8241

References

Arnaud, K. A. 1996, in ASP Conf. Ser., 101, Astronomical Data Analysis Software and Systems V, ed. G. H. Jacoby & J. Barnes (San Francisco, CA: ASP), 17
Bachetti, M. 2015, MaLTPyNT: Quick look timing analysis for NuSTAR data, Astrophysics Source Code Library, ascl:1502.021
Basko, M. M., & Sunyaev, R. A. 1975, A&A, 42, 311
Basko, M. M., & Sunyaev, R. A. 1976, MNRAS, 175, 395
Becker, P. A., Klochkov, D., Schönherr, G., et al. 2012, A&A, 544, A123
Becker, P. A., & Wolff, M. T. 2007, ApJ, 654, 435
Belloni, T. M. 2010, in States and Transitions in Black Hole Binaries, ed. T. Belloni, Vol. 794 (Berlin: Springer), 53
Beloborodov, A. M. 2002, ApJL, 566, L85
Bildsten, L., Chakrabarty, D., Chiu, J., et al. 1997, ApJS, 113, 367
Bird, A. J., Coe, M. J., McBride, V. A., & Udalski, A. 2012, MNRAS, 423, 3663
Burrows, D. N., Hill, J. E., Nousek, J. A., et al. 2005, SSRv, 120, 165
Campana, S., Stella, L., Israel, G. L., et al. 2002, ApJ, 580, 389
Campana, S., Stella, L., Mereghetti, S., & de Martino, D. 2018, A&A, 610, A46
Cappallo, R., Laycock, S. G. T., & Christodoulou, D. M. 2017, PASP, 129, 124201
Cappallo, R., Laycock, S. G. T., Christodoulou, D. M., Coe, M. J., & Zezas, A. 2019, MNRAS, 486, 3248
Cappallo, R. C., Laycock, S. G. T., Christodoulou, D. M., et al. 2020, MNRAS, 495, 2152
Cash, W. 1979, ApJ, 228, 939
Christodoulou, D. M., Laycock, S. G. T., & Kazanas, D. 2018a, MNRAS, 478, 3506
Christodoulou, D. M., Laycock, S. G. T., & Kazanas, D. 2018b, RAA, 18, 128
Christodoulou, D. M., Laycock, S. G. T., & Kazanas, D. 2019, RAA, 19, 146
Christodoulou, D. M., Laycock, S. G. T., Kazanas, D., & Contopoulos, I. 2018c, RAA, 18, 142
Christodoulou, D. M., Laycock, S. G. T., Yang, J., & Fingerman, S. 2017, RAA, 17, 059
Clark, G., Doxsey, R., Li, F., Jernigan, J. G., & van Paradijs, J. 1978, ApJL, 221, L37
Coe, M. J., Bartlett, E. S., Bird, A. J., et al. 2015, MNRAS, 447, 2387
Corbet, R. H. D. 1996, ApJL, 457, L31
Corbet, R. H. D., Marshall, F. E., Coe, M. J., Laycock, S., & Handler, G. 2001, ApJL, 548, L41
Erber, T. 1966, RvMP, 38, 626
Evans, P. A., Beardmore, A. P., Page, K. L., et al. 2007, A&A, 469, 379
Evans, P. A., Beardmore, A. P., Page, K. L., et al. 2009, MNRAS, 397, 1177
Fotopoulou, S., Coe, M. J., Bird, A. J., McBride, V., & Bozzo, E. 2015, ATel, 8207, 1
Frank, J., King, A., & Raine, D. J. 2002, Accretion Power in Astrophysics: Third Edition (Cambridge: Cambridge Univ. Press)
Fürst, F., Kretschmar, P., Kajava, J. J. E., et al. 2017, A&A, 606, A89
González-Galán, A., Oskinova, L. M., Popov, S. B., et al. 2018, MNRAS, 475, 2809
Graczyk, D., Pietrzyński, G., Thompson, I. B., et al. 2020, ApJ, 904, 13
Harrison, F. A., Craig, W. W., Christensen, F. E., et al. 2013, ApJ, 770, 103
Homan, J., & Belloni, T. 2005, Ap&SS, 300, 107
Illarionov, A. F., & Sunyaev, R. A. 1975, A&A, 39, 185
Jaisawal, G. K., & Naik, S. 2016, MNRAS, 461, L97
Jansen, F., Lumb, D., Altieri, B., et al. 2001, A&A, 365, L1
Kahabka, P., & Pietsch, W. 1996, A&A, 312, 919
Kennea, J. A., Burrows, D. N., Coe, M. J., et al. 2015, ATel, 8091, 1
Klus, H., Ho, W. C. G., Coe, M. J., Corbet, R. H. D., & Townsend, L. J. 2014, MNRAS, 437, 3863
Kluzniak, W., & Lasota, J. P. 2015, MNRAS, 448, L43
Koliopanos, F., & Vasilopoulos, G. 2018, A&A, 614, A23
La Palombara, N., Sidoli, L., Pintore, F., et al. 2016, MNRAS, 458, L74
Laycock, S., Corbet, R. H. D., Coe, M. J., et al. 2005, ApJS, 161, 96
Li, K. L., Hu, C. P., Lin, L. C. C., & Kong, A. K. H. 2016, ApJ, 828, 74
Lomb, N. R. 1976, Ap&SS, 39, 447
Lutovinov, A. A., Tsygankov, S. S., Krivonos, R. A., Molkov, S. V., & Poutanen, A. 2017, ApJ, 834, 209
Lyubarskii, Y. É. 1986, Ap, 25, 577
Maitra, C., Paul, B., Haberl, F., & Vasilopoulos, G. 2018, MNRAS, 480, L136
McBride, V. A., Coe, M. J., Negueruela, I., Schurch, M. P. E., & McGowan, K. E. 2008, MNRAS, 388, 1198
Meszaros, P. 1992, High-energy Radiation from Magnetized Neutron Stars (Chicago, IL: Univ. Chicago Press)
Murdin, P., Morton, D. C., & Thomas, R. M. 1979, MNRAS, 186, 43P
Mushtukov, A. A., Suleimanov, V. F., Tsygankov, S. S., & Poutanen, J. 2015, MNRAS, 454, 2539
Negoro, H., Kawamuro, T., Ueno, S., et al. 2015, ATel, 8088, 1
Paul, B., Agrawal, P. C., Rao, A. R., & Manchanda, R. K. 1997, A&A, 319, 507
Postnov, K. A., Gornostaev, M. I., Klochkov, D., et al. 2015, MNRAS, 452, 1601
Reig, P. 2008, A&A, 489, 725
Reig, P., Martínez-Núñez, S., & Reglero, V. 2006, A&A, 449, 703
Reig, P., & Nespoli, E. 2013, A&A, 551, A1
Remillard, R. A., & McClintock, J. E. 2006, ARA&A, 44, 49
Sasaki, M., Haberl, F., & Pietsch, W. 2000, A&AS, 147, 75
Sasaki, M., Müller, D., Kraus, U., Ferrigno, C., & Santangelo, A. 2012, A&A, 540, A35
Savitzky, A., & Golay, M. J. E. 1964, AnaCh, 36, 1627
Scargle, J. D. 1982, ApJ, 263, 835
Schmidtke, P. C., Cowley, A. P., & Udalski, A. 2006, AJ, 132, 971
Schmidtke, P. C., Cowley, A. P., & Udalski, A. 2009, ATel, 1992, 1
Schurch, M. P. E., Coe, M. J., McBride, V. A., et al. 2011, MNRAS, 412, 391
Scowcroft, V., Freedman, W. L., Madore, B. F., et al. 2016, ApJ, 816, 49
Sibgatullin, N. R., & Sunyaev, R. A. 2000, AstL, 26, 699
Staubert, R., Trümper, J., Kendziorra, E., et al. 2019, A&A, 622, A61
Stella, L., White, N. E., & Rosner, R. 1986, ApJ, 308, 669
Strüder, L., Briel, U., Dennerl, K., et al. 2001, A&A, 365, L18

Sturm, R., Haberl, F., Vasilopoulos, G., et al. 2014, MNRAS, 444, 3571
Townsend, L. J., Coe, M. J., Corbet, R. H. D., & Hill, A. B. 2011, MNRAS, 416, 1556
Treiber, H., Vasilopoulos, G., Bailyn, C. D., et al. 2021, MNRAS, 503, 6187
Trümper, J. E., Dennerl, K., Kylafis, N. D., Ertan, Ü., & Zezas, A. 2013, ApJ, 764, 49
Tsygankov, S. S., Doroshenko, V., Lutovinov, A. A., Mushtukov, A. A., & Poutanen, J. 2017, A&A, 605, A39
Tsygankov, S. S., Lutovinov, A. A., Doroshenko, V., et al. 2016a, A&A, 593, A16
Tsygankov, S. S., Lutovinov, A. A., & Serber, A. V. 2010, MNRAS, 401, 1628
Tsygankov, S. S., Mushtukov, A. A., Suleimanov, V. F., & Poutanen, J. 2016b, MNRAS, 457, 1101
Udalski, A., Szymanski, M. K., Soszynski, I., & Poleski, R. 2008, AcA, 58, 69
Udalski, A., Szymański, M. K., & Szymański, G. 2015, AcA, 65, 1
Vasilopoulos, G., Haberl, F., Carpano, S., & Maitra, C. 2018, A&A, 620, L12
Vasilopoulos, G., Haberl, F., & Maggi, P. 2017, MNRAS, 470, 1971
Vasilopoulos, G., Ray, P. S., Gendreau, K. C., et al. 2020, MNRAS, 494, 5350
Wang, Y. M., & Frank, J. 1981, A&A, 93, 255
Wang, Y. M., & Welter, G. L. 1981, A&A, 102, 97
Wasserman, I., & Shapiro, S. L. 1983, ApJ, 265, 1036
Yang, J., Laycock, S. G. T., Christodoulou, D. M., et al. 2017, ApJ, 839, 119
Yang, J., Zezas, A., Coe, M. J., et al. 2018, MNRAS, 479, L1
Yokogawa, J., Imanishi, K., Tsujimoto, M., Koyama, K., & Nishiuchi, M. 2003, PASJ, 55, 161
Yokogawa, J., Torii, K., Kohmura, T., & Koyama, K. 2001, PASJ, 53, 227